AGU PUBLICATIONS

Water Resources Research

RESEARCH ARTICLE
10.1002/2015WR018111

Free phase gas processes in a northern peatland inferred from autonomous field-scale resistivity imaging

Neil Terry[1], Lee Slater[1], Xavier Comas[2], Andrew S. Reeve[3], Karina V. R. Schäfer[4], and Zhongjie Yu[5]

[1]Department of Earth and Environmental Sciences, Rutgers—State University of New Jersey, Newark, New Jersey, USA, [2]Department of Geosciences, Florida Atlantic University, Boca Raton, Florida, USA, [3]School of Earth and Climate Sciences, University of Maine, Orono, Maine, USA, [4]Department of Biological Sciences, Rutgers—State University of New Jersey, Newark, New Jersey, USA, [5]Department of Geology and Planetary Science, University of Pittsburgh, Pittsburgh, Pennsylvania, USA

Key Points:
- Field-scale autonomous resistivity imaging is used to infer gas content changes in peat
- Pressure decreases cause bubble expansion and rapid drops trigger ebullition
- Findings support shallow and deep peat models in terms of biogenic gas release from peat soils

Supporting Information:
- Supporting Information S1
- Movie S1

Correspondence to:
N. Terry,
neil.terry@rutgers.edu

Citation:
Terry, N., L. Slater, X. Comas, A. S. Reeve, K. V. R. Schäfer, and Z. Yu (2016), Free phase gas processes in a northern peatland inferred from autonomous field-scale resistivity imaging, *Water Resour. Res.*, *52*, 2996–3018, doi:10.1002/2015WR018111.

Received 14 SEP 2015
Accepted 20 MAR 2016
Accepted article online 23 MAR 2016
Published online 21 APR 2016

Abstract The mechanisms that control free phase gas (FPG) dynamics within peatlands, and therefore estimates of past, present, and future gas fluxes to the atmosphere remain unclear. Electrical resistivity imaging (ERI) is capable of autonomously collecting three-dimensional data on the centimeter to tens of meter scale and thus provides a unique opportunity to observe FPG dynamics in situ. We collected 127 3-D ERI data sets as well as water level, soil temperature, atmospheric pressure, and limited methane flux data at a site in a northern peatland over the period July–August 2013 to improve the understanding of mechanisms controlling gas releases at a hitherto uncaptured field scale. Our results show the ability of ERI to image the spatial distribution of gas accumulation and infer dynamics of gas migration through the peat column at high (i.e., hourly) temporal resolution. Furthermore, the method provides insights into the role of certain mechanisms previously associated with the triggering of FPG releases such as drops in atmospheric pressure. During these events, buoyancy-driven gas release primarily occurs in shallow peat as proposed by the "shallow peat model." Releases from the deeper peat are impeded by confining layers, and we observed a large loss of FPG in deep peat that may likely represent a rupture event, where accumulated FPG escaped the confining layer as suggested by the "deep peat model." Negative linear correlations between water table elevation and resistivity result from hydrostatic pressure regulating bubble volume, although these variations did not appear to trigger FPG transfer or release.

1. Introduction

Methane (CH_4) is the third most abundant greenhouse gas in the atmosphere but has 34 times the heat trapping potential of water vapor [*Forster et al*., 2007]. Wetlands, and peatlands in particular, are major sources of CH_4 and account for approximately 22% of the global CH_4 flux to the atmosphere [*Stocker et al*., 2013]. In addition, global warming is anticipated to further stimulate CH_4 production from these ecosystems, creating a positive feedback loop [*Bridgham et al*., 2013].

Despite the known significance of wetlands with respect to climate change, the 2013 Intergovernmental Panel on Climate Change report [*Stocker et al*., 2013] states that confidence in modeled CH_4 flux from wetlands remains low, owing to a lack of observational data sets for calibration of process-based models [i.e., *Hodson et al*., 2011; *Ringeval et al*., 2011; *Spahni et al*., 2011]. The spatial and temporal variability in CH_4 production, transport, and release within these wetlands also remains poorly constrained [*Papa et al*., 2010].

CH_4 is produced in peatlands primarily by microbes and is released to the atmosphere through diffusion, transport through vascular plants, and/or rapid ebullition (bubbling). The overall CH_4 produced by these microbes and the subsequent release to the atmosphere are controlled by a number of biological and environmental factors. A considerable body of research has been dedicated to linking these factors to CH_4 flux in order to understand the current and future response of peatlands to climate change. *Walter and Heimann* [2000] developed a process-based model for estimating methane emissions from wetlands that includes diffusion, transport, and ebullition mechanisms. However, this model lacks a bubble dynamics component. In order to better understand the relationship between bubble dynamics and ebullition, there is a need for observational data sets at high spatiotemporal resolution.

Direct chamber-based measurements of CH_4 fluxes typically have a small (< 1 m^2) footprint that may not be suitable for upscaling, whereas eddy covariance systems integrate over a much larger area but may not have the required resolution to capture short-term ebullition events, which can episodically release a large amount of CH_4 over a short time period [*Rosenberry et al*., 2006]. In a recent study, *Gålfalk et al*. [2015] developed an optimized infrared hyperspectral imaging system capable of photographing CH_4 at the sub-m^2 scale that offers great promise to bridge-scale differences between chamber measurements and eddy covariance systems. In a laboratory study of a peat monolith, *Yu et al*. [2014] recorded 926 ebullition events lasting minutes to hours, which released CH_4 at a rate of 212.2 ± 44.3 mg m^{-2} d^{-1} during a single event. *Glaser et al*. [2004], relying on peat deformation and hydraulic head measurements, calculated a loss of 130 g m^{-2} of CH_4 over three individual ebullition events believed to originate deep (>4 m) in the peat profile during the late summer from the Glacial Lake Agassiz peatlands (GLAP) in Northern Minnesota. This result, when averaged over an entire year, is an order of magnitude larger than the diffusive rate based on seasonal chamber measurements from the same site [*Chasar*, 2002].

Such results and the observations of others [*Chanton et al*., 1995; *Chasar*, 2002; *Chasar et al*., 2000a,b; *Crill et al*., 1988, 1992; *Romanowicz et al*., 1993, 1995; *Rosenberry et al*., 2003; *Siegel et al*., 2001] formed the basis for the so-called "deep peat model" [*Glaser et al*., 2004]. This model stresses extensive CH_4 production in "hotspots" within the most anaerobic deep peat ($>$ 3 m) [*Siegel et al*., 2001] due to readily available labile C substrate transported from above. When equilibrium is disrupted, such as by changes in atmospheric pressure [*Comas et al*., 2011a], gas migrates upward due to increased buoyancy. Gas bubbles that are trapped under confining layers are episodically released in large concentrations when confining forces are exceeded by buoyancy forces associated with bubble expansion during abrupt drops in atmospheric pressure [*Rosenberry et al*., 2003; *Glaser et al*., 2004]. However, increases in atmospheric pressure have also been correlated with increased fluxes in deep parts of the peat column in northern systems and in shallow peat along subtropical systems [*Comas et al*., 2011a, *Comas and Wright*, 2014].

The "shallow peat model" proposed by *Coulthard et al*. [2009] instead suggests that most biogenic gas production, and particularly CH_4, likely occurs in the shallow (<1 m) anaerobic zone, driven by higher summer temperatures [*Dunfield et al*., 1993], more abundant labile C [*Moore and Dalva*, 1993], and trapped bubbles acting as nucleation sites for CH_4 during water table rise [*Beckwith and Baird*, 2001]. This model holds that FPG buildup and episodic ebullition are common in the shallow peat, and may contribute more to FPG flux than less frequent ebullition events from deep layers. *Coulthard et al*. [2009] base their model on the large body of literature on methane production and bubble formation in shallow peat [e.g., *Baird et al*., 2004; *Beckwith and Baird*, 2001; *Christensen et al*., 2003; *Comas and Slater*, 2007; *Kellner et al*., 2006; *Laing et al*., 2008; *Ström et al*., 2005; *Tokida et al*., 2005]. However, they stress that improved direct observation of deep FPG dynamics is required to confirm the relative importance of deep peat to ebullition.

Geophysical methods provide a unique opportunity to study three-dimensional FPG dynamics below the peat surface at spatial scales ranging from centimeters to tens of meters. Measurements can be made noninvasively, without disturbing the internal structure of the peat and therefore altering the naturally existing gas dynamics. In contrast, direct measurements made by installing wells or inserting probes into peat can immediately create a vent for gas to escape and potentially leave a preferential flow pathway for gas to migrate along thereafter [*Rosenberry et al*., 2006]. Ground penetrating radar (GPR) has been extensively employed as an indirect and minimally invasive methodology for determining temporal variations in FPG content in peatlands [*Comas et al*., 2005, 2011a; *Parsekian et al*., 2010, 2011; *Strack and Mierau*, 2010] at both laboratory and field scales. Here "minimally invasive" implies that although there is some disturbance to the peat surface from walking over it with antennas, no disturbance of the internal structure of the peat is necessary. GPR wave velocities are very sensitive to moisture content, and can hence be used to qualitatively and semiquantitatively assess changes in FPG content [*Comas et al*., 2008]. As previously mentioned, the minimally invasive nature of GPR offers a critical advantage when seeking to avoid disruption of the natural FPG dynamics within peatlands. However, GPR is not ideal as a long-term monitoring tool as it is not readily automated, particularly at the field scale.

Electrical resistivity imaging (ERI) is another minimally invasive geophysical technique that potentially can be used to indirectly monitor FPG in peat, as the degree of saturation (and therefore amount of gas) influences the bulk resistivity of the peat. Unlike GPR, which relies on field operators to acquire subsequent data sets, ERI can be completely automated to collect time-lapse 3-D data [e.g., *Daily et al*., 2004; *Singha et al*.,

2014, for review]. Two laboratory studies have previously highlighted the potential of ERI for assessing FPG dynamics in peat. *Slater et al*. [2007] demonstrated the utility of electrical imaging to monitor time-lapse changes in gas content in a single laboratory peat monolith and *Kettridge et al*. [2011] extended this approach to study biogenic gas dynamics in several peat cores reflecting different peat types and meteorological conditions. Both these laboratory studies concluded that a quantitative assessment of FPG content and/or flux is unrealistic using ERI, but that this technique is effective at capturing changes in gas content in peat and for inferring the mechanisms driving these changes. However, a field-scale application of this approach has not yet been undertaken.

In this study, we report on the first attempt to apply time-lapse ERI to monitor biogenic gas dynamics at the field scale. Time-lapse ERI data sets are compared with a shorter duration set of direct high temporal resolution measurements of CH_4 flux to further evaluate the driving forces behind FPG dynamics and ebullition. We show how ERI data sets provide valuable insights into the processes regulating CH_4 bubble transport and ebullition at a unique spatial-scale hitherto unachieved with other investigation techniques. Our results give large-scale information on the role of atmospheric pressure and water levels variations on gas release and demonstrate that major episodic ebullition events associated with large pressure drops are clearly associated with changes in gas content throughout the peat profile. These results also offer clear insights into the relative importance of shallow versus deep sources of CH_4 releases via ebullition release regulated by atmospheric pressure and water level. Our analysis supports the shallow peat model in that the release of gas from the upper meter of peat appears to be more common than below 1 m. However, ERI data from this study also support the deep peat model as we witnessed one large ebullition event originating from deep peat below a woody layer. This work has implications for better understanding how climate-induced changes in pressure, rainfall, and temperature may increase greenhouse gas release from peat soils.

2. Background

2.1. Electrical Resistivity Imaging (ERI)

ERI surveys involve driving a known current (normally using a modified low-frequency square wave) between two electrodes and measuring the potential difference between other pairs of electrodes at multiple locations. Raw ERI data thus consist of transfer resistances, which are simply the potential differences divided by the injected current (Ohm's law). In a homogenous medium, resistivity can be computed analytically using the positions of the electrodes and the transfer resistance. Heterogeneous resistivity distributions require inverse methods to arrive at a solution (see *Binley and Kemna* [2005] for further details). Historically, ERI was primarily used for geologic characterization and natural resource exploration, but application of ERI to study near-surface dynamic processes via time-lapse imaging is now well established (see *Singha et al*. [2014] for a recent review). Electrical resistivity has been used as a proxy for time-varying parameters of interest including moisture content [*Binley et al*., 2002], salinity [*Hayley et al*., 2009], and temperature [*Krautblatter and Hauck*, 2007]. Well-established petrophysical relations link resistivity to certain physical and chemical properties of the pore space. As we will discuss, however, it is often impossible or impractical to establish such a link under field conditions.

The measured bulk resistivity (1/conductivity) of a metal-free soil consists of the combined effects of electrolytic conduction (ions in the solution filling the interconnected pore space) and surface conduction (ions in the electrical double layer at the walls of the connected pores) pathways, which add in parallel. Ignoring surface conduction, the resistivity of a soil (ρ_{soil}) can be modeled using Archie's law for unsaturated sediments,

$$\frac{1}{\rho_{soil}} = \sigma_{el} = (\phi_{int})^m S^n \sigma_w, \tag{1}$$

where σ_{el} is the electrolytic conduction pathway representing the flow of current through ions in the pore fluid, ϕ_{int} is the interconnected porosity, S is saturation, σ_w is the conductivity of the pore fluid, m is the "cementation" factor which depends on pore structure and tortuosity, and n is the saturation exponent describing the distribution of air in pore spaces and is dependent on soil type.

Archie's law may be poorly parameterized for organic soils, and alternative formulations linking resistivity to the soil property of interest may be needed. Archie's law assumes (1) no surface conduction, which will

certainly be violated in organic soils of large surface area saturated with pore fluids of low ionic concentrations as is typical of ombrotrophic bogs, and (2) a nonconducting soil matrix, which may also be violated in organic sediments as there is evidence for electronic conduction occurring across organic particles themselves [*Comas and Slater*, 2004]. In addition, peat soils exhibit a strong dependence of ϕ_{int} on σ_w [*Comas and Slater*, 2004] likely due to pore dilation resulting from the flocculation of organic acids on macropore surfaces [*Ours et al*., 1997]. *Comas and Slater* [2004] found an empirical power law relationship linking ρ_{soil} to surface conductivity and σ_w.

Slater et al. [2007] used a time-lapse inversion approach to highlight changes in resistivity that they associated with changes in *S* due to biogenic gas production, gas transport, and subsequent release from peat soils. While resistivity values were corrected for changes in σ_w, *Slater et al*. [2007] assumed negligible surface conduction effects and insignificant temporal changes in the Archie exponents *m* and *n* to use the following relationship,

$$S=\frac{\theta}{\phi}=\frac{(\phi-FPG)}{\phi}=\left[\frac{\rho_{[unsat]}}{\rho_{[sat]}}\right]^{-1/n}, \tag{2}$$

where θ is the water content, ϕ is the total porosity, *FPG* is free phase gas content, and $\rho_{[unsat]}$ and $\rho_{[sat]}$ are the resistivity of the soil in unsaturated and completely saturated conditions, respectively. Time-lapse resistivity was thus related to relative changes in FPG content through comparison of their ratios,

$$\rho_{rat}=\frac{\rho_{soil,t}}{\rho_{soil,0}}=\left[\frac{\phi_t-FPG_t}{\phi_0-FPG_0}\right]^{-n}, \tag{3}$$

where ρ_{rat} is referred to as the ratio resistivity, $\rho_{soil,0}$, ϕ_0, FPG_0, $\rho_{soil,t}$, ϕ_t, and FPG_t are the resistivity, porosity, and free phase gas content of the soil at time 0 and *t*, respectively. In the *Slater et al*. [2007] study, porosity variations were monitored through elevation rod measurements, while *n* and FPG_0 values were estimated from a parallel block experiment [*Comas and Slater*, 2007].

Controlled laboratory conditions allowed quantification of FPG in the study of *Slater et al*. [2007], but it is likely impractical to establish any such quantitative link between resistivity and gas content in the field. Application of equation (3) at the field-scale requires spatiotemporal information on the variation of porosity, the saturation exponent, and an initial estimate of the free phase gas content. Estimation of FPG_0 through evaluation of equation (1) in turn requires information on interconnected porosity, the cementation exponent, and pore water conductivity. An assumption that surface conduction effects are negligible and that the peat matrix acts as a pure insulator is also needed. Given these limitations, we restrict our analysis to ratio resistivity, and abandon the idea of quantitatively predicting gas content/changes from the images. *Johnson et al*. [2012] stress the utility of geophysics, and ERI in particular, for capturing the inherent hydrogeological responses within geophysical data without the need to explicitly reconstruct hydrogeological properties from the geophysical data. Following their lead, we use ERI to capture spatiotemporal dynamics of gas releases as a function of environmental forcing without attempting to estimate physical properties given the likely futility of the approach in such an electrically complex porous medium. We recognize that peat is a highly compressible material whose physical properties may vary through time and that we cannot necessarily attribute all changes in ERI data to changes in gas content. However, we assume these changes are negligible in our case when considering the scale difference between our gas content estimates, which are based on the entire thickness of the peat column (over 6 m thick within our study area), and typical changes in vertical deformation due to matrix contraction and expansion (i.e., only as high as 0.02–0.03 m for shallow portions of the column as recorded from other studies at the same peatland unit [*Comas et al*., 2011a]).

2.2. Time-Lapse Inversion of ERI Data

Inverse methods are needed to estimate the distribution of model parameters from boundary observations. This problem is ill posed for ERI data where many resistivity distributions may satisfy the data. We used R3t (Andrew Binley, Lancaster University) to invert the ERI data. In R3t, forward data are numerically simulated by evaluating the 3-D Poisson equation using the finite element method. For inversion, R3t iteratively minimizes an objective function of the general form,

$$\Psi_{total} = \Psi_d + \alpha \Psi_m, \quad (4)$$

where Ψ_d is the data misfit, Ψ_m is the model misfit, and α is a regularization term penalizing departure from a starting model. At each iteration, model parameters (resistivity of mesh elements) are updated through a Gauss-Newton approach, with α optimized through a line search at each Gauss-Newton iteration. Convergence is gauged by the root-mean-squared error of the data misfit normalized by a user-supplied estimate of the data error. It is therefore critical to supply quantitative estimates of the errors in the field data to the inversion routine to avoid overfitting or underfitting the data which can result in image artifacts unrelated to the subsurface resistivity structure [*LaBrecque et al*., 1996]. For more information on the theory of inverse methods for ERI, see *Binley and Kemna* [2005].

Although it is possible to simply compare resistivity images postinversion through division or subtraction, time-lapse ERI data can be "differenced" prior to inversion to enhance the sensitivity of the inverse procedure to changes in the data [*Labrecque and Yang*, 2001]. Changes in resistivity are highlighted through this approach by modification of data input into the inverse routine,

$$\mathbf{d}_{diff,i} = \mathbf{d}_i + \mathbf{d}_f - \mathbf{d}_0, \quad (5)$$

where $\mathbf{d}_{diff,i}$ are the differenced resistance data, $\mathbf{d}_i$ are the observed data, $\mathbf{d}_0$ are the resistance data from a reference data set in time, and $\mathbf{d}_f$ are theoretical resistances for a forward model for that reference data set. Here the subscript i refers to the time index of each data set. Following standard rules of error propagation, the total errors $\boldsymbol{\varepsilon}_i$ required to weight each measurement in the inversion appropriately are then,

$$\boldsymbol{\varepsilon}_{diff,i} = \sqrt{\boldsymbol{\varepsilon}_i^2 + \boldsymbol{\varepsilon}_f^2 + \boldsymbol{\varepsilon}_0^2}, \quad (6)$$

where $\boldsymbol{\varepsilon}_{diff,i}$ are the errors put into the difference inversion, $\boldsymbol{\varepsilon}_i$ are observed data errors, $\boldsymbol{\varepsilon}_f$ are the forward modeling errors (calculated through forward modeling of a 100 ohm m homogeneous medium), and $\boldsymbol{\varepsilon}_0$ are the errors for the background data set. The absolute percent differences between the data computed in R3t for a homogenous medium and the analytically calculated transfer resistances for the same homogeneous medium are multiplied by $\mathbf{d}_{diff,i}$ and used as $\boldsymbol{\varepsilon}_f$.

2.3. Analysis of ERI Time Series

Comprehensively representing the information content in large time-lapse ERI data sets can be challenging given that it is impractical and often not informative to present a large number of images (in this study, there are 127 raw data sets). *Singha et al*. [2014] outline several strategies for analyzing time series ERI data. *Johnson et al*. [2012] investigated correlations, cross correlations, and time lag to maximum correlation between the resistivity time series at individual voxels (different spaces in the modeled domain) and environmental variables to derive hydrologic information on controls on groundwater-surface water exchange. We adopt a similar approach to help draw out information on the environmental parameters driving variation in FPG content in peat.

Linear correlations can be calculated using Pearson's correlation coefficient, r.

For convenience of discussion, we employ the following nomenclature for describing the strength of r: $0.0 \leq |r| < 0.1$ = none, $0.1 \leq |r| < 0.4$ = weak, $0.4 \leq |r| < 0.7$ = moderate, $0.7 \leq |r| < 1.0$ = strong.

3. Methodology

3.1. Study Site: Caribou Bog, Maine

Caribou bog is a 2200 ha multiunit ombrotrophic peatland in central Maine. The central unit of the bog wherein this study was performed lies between Pushaw Lake and the Penobscot River, and features a well-developed pattern of pools and raised bog complexes [*Davis and Anderson*, 1999]. Using a combination of direct measurements and indirect geophysical measurements, *Slater and Reeve* [2002] and *Comas et al*. [2011b] identified the peat layer of the bog as having a variable thickness of less than 12 m in most locations, overlying a discontinuous layer of organic-rich lake sediment exceeding 5 m in certain areas [*Comas and Slater*, 2004]. The underlying mineral basement consists of the Presumpscot Formation; a glacio-marine silt-clay layer overlying glacial till resulting from erosion of bedrock during the Pleistocene

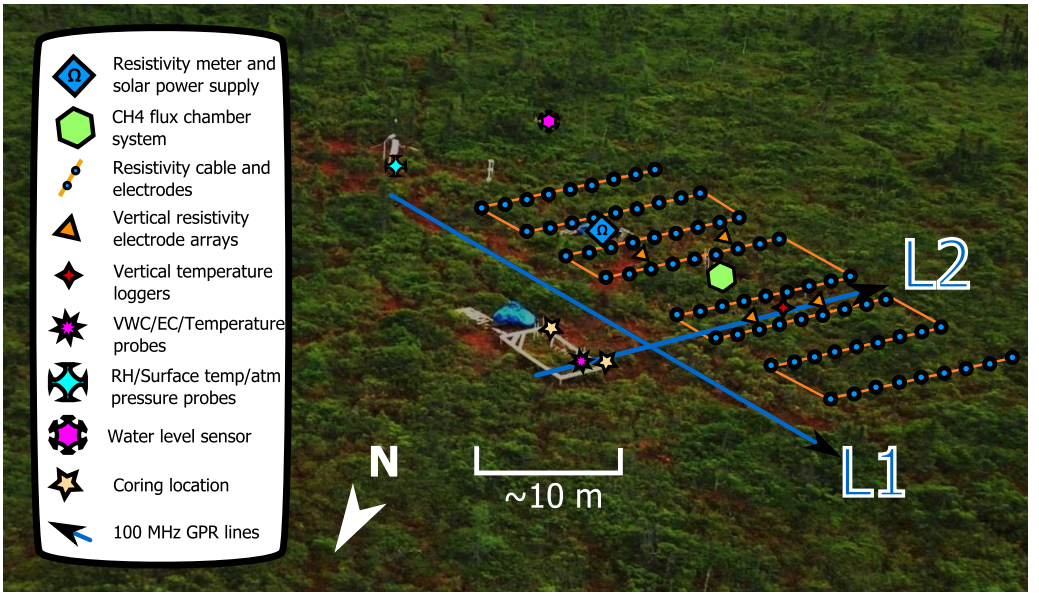

Figure 1. Schematic of the ERI resistivity array and relevant sensors overlain on a satellite image. GPR L2 corresponds to Figure 3e.

[*Bloom*, 1963]. The bedrock consists of metamorphosed middle Ordovician to middle Devonian material [*Osberg et al*., 1985].

This study focuses on an area within the Central unit of Caribou bog vegetated primarily with small-leaved *Sphagna* including *Sphagnum capillifolium* (Ehrh.) Hedw. and *Sphagnum fuscum* (Schimp.) Klinggr. This particular site was chosen as part of a larger research project investigating FPG dynamics as a function of land cover type, including: pools, shrub, and wooded heath (this study). Overlying the *Sphagna* are several low ericaceous shrubs, mainly *Chamaedaphne calyculata* (L.) Moench. A few isolated tall evergreen trees are also present outside the footprint of the ERI survey.

3.2. Field Implementation of ERI

A schematic of the ERI monitoring array and associated sensors is shown in Figure 1, and Table 1 is a summary of these data along with estimated sampling volume, spatiotemporal resolution, and accuracy/precision. Automated ERI data collection used an IRIS Syscal Pro Switch resistivity instrument with two solar circuits to power a transmitter and a receiver/field computer. Complete data sets were collected from 4 July 2013 to 28 August 2013 for a total of 127 time-lapse data sets with a minimum time step of 2 h and an average of 10 h between them. The system employed 72 stainless steel electrodes that covered a 28 by 10 m area. Electrodes were arranged in eight lines with 1.25 m within line spacing and variable spacing (3.5–5 m) between lines to accommodate other instrumentation. The measurement scheme consisted of a nonstandard dipole-dipole array, with an intradipole (a) spacing of 1 and 8 electrodes, and an inter-dipole spacing (na) from 1 to 68 electrodes for a total of 2184 unique measurements at each data collection time. Given the total size of the ERI array (28 m by 10 m), the maximum distance between dipole centers is 27.8 m. Using the common convention of estimating pseudodepth for dipole-dipole arrays by the intersection of 45° lines drawn down from the dipole centers, this equates to an investigation depth of 13.9 m. This depth is likely quite exaggerated. Therefore, we performed forward and inverse modeling experiments (shown in supporting information) to confirm the array is sensitive to relatively small changes in resistivity throughout the entire peat profile (down to 6.4 m depth at this site).

Full reciprocal measurements (current and potential electrodes switched) for each data set were also gathered for error analysis purposes. The reciprocity principle states that an electric field will remain the same if current and potential measurement locations are reversed. To optimize current injections and data collection speed, several "dummy" measurements were added. Thus, 4984 data were collected at each time step, including a full set of reciprocal measurements. Each data set took approximately 1 h and 15 min to collect

Table 1. Summary of Data Collected

Method (Type of Data Collected)/Instrument Used	Sampling Volume/Spatial Resolution	Temporal Resolution (Highest)/Time Period Collected	Instrument Accuracy/Precision
ERI (resistance)/IRIS SyscalPro	>1000 m^3 sampling volume/<1 m^3 spatial resolution	2 h/July and August 2013	$\pm$0.2% accuracy ±1 μV precision
VEA (resistance)/Campus Geopulse Tigre	>1 m^3 sampling volume/<1 m^3 spatial resolution	24 h/July 2013	$\sim\pm$1% accuracy
GPR (EM wave travel times and amplitudes)/MALA ProEx	>100 m^3 sampling volume/<1 m^3 spatial resolution	Single measurement/3 July 2013	$\sim\pm$0.001 m/ns precision
Dynamic flux chamber (CH_4 concentration)/Licor LI-7700	<1 m^2/point measurement	1 s/select periods during July 2013	$\pm$5 ppb accuracy
Temperature logging/HOBO pendants	~1 cm^3/point measurement	15 min/July and August 2013	$\pm$0.53°C accuracy $\pm$0.14°C precision
Electrical conductivity logging/Decagon 5TE	~10 cm^3/point measurement	1 min/July and August 2013	$\pm$10% (EC accuracy)/$\pm$3% (VWC accuracy)
Pressure transducer (water level)/Solinst LevelLogger Junior 3001	~1 cm/point measurement	2 min/July and August 2013	±1 cm accuracy
Atmospheric pressure/surface temperature/relative humidity logging/Hydroinnova cosmic-ray probe	~1 cm^3/point measurement	1 h/July and August 2013	$\pm$0.1 hPa (atmospheric pressure accuracy) ±1°C (temperature accuracy) $\pm$3% (relative humidity accuracy)

using three stacks and a 500 ms time delay between current injections. Voltage injection was set at 100 V, providing a good compromise between signal-to-noise ratio and power consumption.

Four vertical electrode arrays (VEAs) each with 16 electrodes spanning from the surface to the mineral soil were installed with electrodes spaced 0.3 m apart at different locations within the resistivity array (Figure 1). Data were collected in a Wenner configuration using a Campus Geopulse resistivity instrument once daily during most of July 2013, but were not gathered during the August monitoring period. These data were primarily collected to add confidence to our 3-D ERI inversion results. Given the decaying sensitivity of ERI inversions away from the electrodes, the VEAs provide reassurance (in addition to that from resolution matrix and depth of investigation statistics) that measurements in low-sensitivity areas (i.e., the deep peat) are reliable.

3.3. Supporting Environmental and Geophysical Data

Environmental sensors installed included nine HOBO pendant soil temperature loggers spanning from just below the peat surface to 6.4 m depth at 0.8 m intervals (primarily intended to correct resistivity inverse results for temperature variations throughout the peat profile; data logged every 15 min), a Solinst LevelLogger Junior 3001 water level sensor (primarily for observing the link between resistivity, water level and gas dynamics; collected at 2 min intervals), and a relative humidity/air temperature/atmospheric pressure sensor (built into a Hydroinnova Cosmic-ray moisture probe; collected at 1 h intervals). Water levels were compensated for atmospheric pressure variations using a sensor built in to the logger. The relative humidity/air temperature/atmospheric pressure information was mainly used to perform corrections to methane flux data (described later in this section), as well as to study the relationship between atmospheric pressure and gas dynamics. The locations of the environmental sensors are shown in Figure 1. Daily rainfall data were taken from the local weather underground station in Bangor, ME (KMEBANGO3). Four Decagon 5TE probes were installed at various depths to monitor bulk electrical conductivity, 1 min data collection interval. These probes also recorded dielectric permittivity and temperature, which in addition to the bulk electrical conductivity, were used to estimate changes in pore water conductivity (described below). The layout of these sensors is shown in Figure 1, and a summary of the types of data collected is shown in Table 1.

A key assumption of our resistivity monitoring experiment is that the effect of changing pore water conductivity σ_w remains small compared to the effect of changing FPG content. Using the conversion presented in the 5TE manual and the relationships described by *Hilhorst* [2000], we converted bulk conductivity, bulk

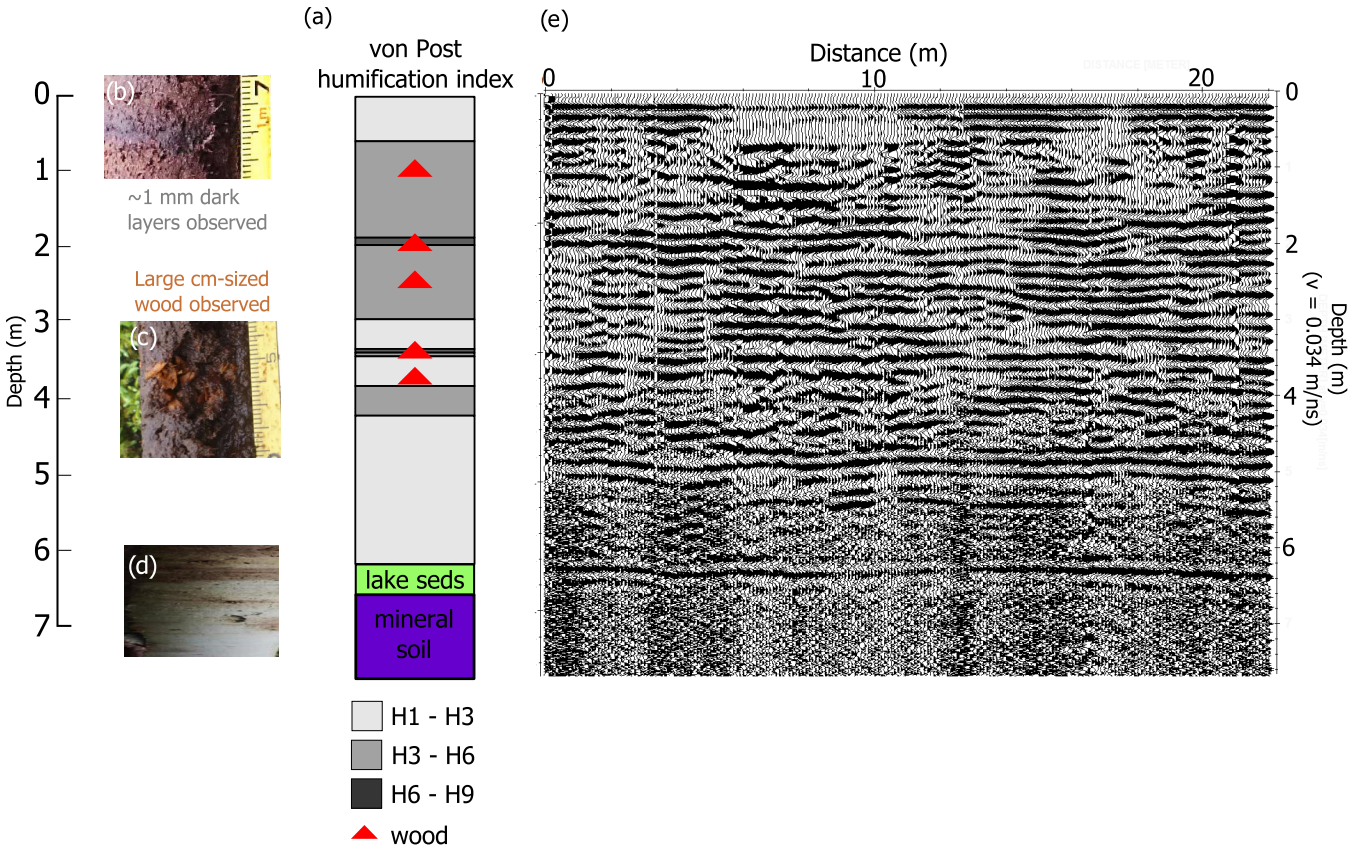

Figure 2. Preliminary characterization of the Caribou Bog site: (a) von Post humification index and select features along the 7.0 m core identified in the field; (b) photograph of example dark layer; (c) photograph of example woody debris observed; (d) photograph of the transition from peat to the lake sediment at 6.4 m; (e) ground penetrating radar (GPR) line taken nearby which shows the peat/mineral soil interface as a clear reflector at 6.4 m.

dielectric permittivity, and temperature to σ_w at 0.2, 1.0, 3.0, and 4.5 m depth. We recognize that this conversion factor is based on assumptions that are likely violated for organic peat soils and therefore focus our interpretation on the relative variation at each probe.

GPR data were collected along two profiles (shown in Figure 1b) using a MALA ProEx system and 100 MHz unshielded antennas. The data underwent basic processing including (1) dewow, (2) time-zero adjustment, (3) exponential gain, and (4) trimming of the profiles to include only the data near the core and resistivity array. For time to depth conversion, a common midpoint survey and subsequent analysis revealed an average EM velocity of 0.034 m/ns, within 0.001 m/ns of values previously reported for Caribou Bog (for example, by *Comas et al.* [2005, 2011a]). Limited CH_4 flux data were recorded during the month of July by a dynamic flux chamber system located in the center of the ERI array (location shown in Figure 1b). The flux chamber system consists of a modified form of the setup employed by *Mastepanov and Christensen* [2009] and similar to the laboratory configuration of *Yu et al.* [2014] whereby an open path fast CH_4 analyzer (FMA, LI-7700, LI-COR Biosciences, Lincoln, NE, USA) is enclosed in a plastic chamber to continuously monitor CH_4 concentrations. The setup is equipped with a pump to circulate air through the system. Due to power limitations at the remote fieldsite, the CH_4 flux data were only acquired over five monitoring periods lasting from 1 to 3 days each at high (1 s) temporal resolution. Raw measurements were adjusted for variations in pressure, temperature, and relative humidity according to Webb-Pearman-Leuning (WPL) [*Webb et al.*, 1980] and spectroscopic corrections [*McDermitt et al.*, 2011] before converting to CH_4 flux.

3.4. Initial Subsurface Characterization

Initial characterization of the site was based on two cores (locations shown in Figure 1). A von Post humification test was performed for the western core only (Figure 2a). The von Post humification scale is a set of

guidelines for identifying the relative degree of peat composition in the field (1 being the least decomposed and 10 being completely decomposed).

Both cores revealed an approximately 6.4 m thick peat layer overlying a 0.4 m transition zone of lake sediment (pictured in Figure 2d) becoming pure glaciomarine clay mineral soil at 6.8 m depth. Layers of poorly decomposed wood debris were identified at approximately 1.9, 3.45, and 3.75 m depth in the western core and at 2.3 and 3.45 m depth in the eastern core as shown in Figure 2c. The woody layers correspond to distinct decreases in von Post humification (Figure 2a). In addition, several ~1 mm dark layers, likely ash or possibly layers of enhanced peat decomposition, were visible between 1 and 2 m depth in both cores (Figure 2b).

Data from one of the GPR lines (shown as L2 in Figure 1) collected at the site are displayed in Figure 2e and show distinct reflection events from the mineral sediment and numerous semicontinuous reflectors in between, likely associated with woody debris. This GPR radargram, combined with that obtained on a second line (not shown here for brevity), confirm that the mineral soil is mostly flat but grades slightly downward toward the south (0.4% and 0.5% gradient estimated toward the southeast and southwest in lines 1 and 2, respectively). Furthermore, it confirms the lateral continuity of some of the stratigraphic attributes described above (i.e., woody layers at 1.9 and 3.75 m depth as well as the peat-mineral soil interface at 6.4 m).

3.5. ERI Data Processing and Time Series Analysis

3.5.1. Data Filtering

For quality control purposes, all measurements from the time series with (1) >25% reciprocal error, (2) a negative resistivity, or (3) an applied current or measured voltage of less than 1 mV or 1 mA were removed (performed after data collection; there was no field filtering of data). Reciprocal error percentage was calculated as the normal measurement minus the reciprocal measurement, all divided by the normal measurement. In the raw data, normal-reciprocal errors were highly left-skewed and averaged 6% due primarily to a relatively small number of measurements (~3%) possessing large reciprocal errors. The choice of a 25% reciprocal error and 1 mV cutoff was based on the relatively low electrical noise at the field site in Caribou Bog.

To make each data set comparable to the next for time-lapse inversion, measurements failing to meet these conditions within a particular data set were removed from all data sets in the time series. Under these criteria, each data set retained 3338 of the 4984 original measurements (67%). In other words, there were 1669 normal measurements and 1669 reciprocal measurements for each time series data set after the filtering. The remaining data exhibited a mean reciprocal error of 0.46%. Within each data set, the averages of the normal and reciprocal measurements were used for inversion.

3.5.2. Mesh Design

A tetrahedral finite element method mesh was designed in GMSH [*Geuzaine and Remacle*, 2009] and was extended 60 m away from electrodes to establish Neumann (no electrical current flow) boundary conditions. Elements at the electrodes were assigned a characteristic length of one fourth the minimum interelectrode distance (0.3125 m) to ensure adequate forward modeling of electrical potentials near the electrodes, while the characteristic length at boundaries was set at 25 m. Elements in between the electrodes and the boundaries gradually spanned lengths in between these two sizes, consistent with the decaying sensitivity of ERI data away from the electrodes. An additional optimization step was performed in GMSH to remove ill-conditioned elements (slivers, caps, splinters, and wedges) [*Cheng et al.*, 1999]. In total, this produced a mesh with 47,722 voxels and 11,863 nodes.

3.5.3. Error Modeling and Propagation

A forward model of a homogeneous medium was run to assess numerical errors ε_f, while machine precision errors were considered negligible in this study. Forward modeling errors were very small (maximum error of less than 0.015 ohm m), owing to the singularity removal procedure [*Lowry et al.*, 1989] applied in R3t. Singularity removal requires that the surface of the FEM mesh be completely flat. Although our study area was located on a hummock and hollow area of Caribou bog, the maximum topographic variation (0.21 m) among electrodes was smaller than the characteristic length of the smallest element in the FEM mesh. Therefore, we did not consider this microtopography in our inversion.

We used the binning approach of *Koestel et al.* [2008] to build a data error model based on reciprocal errors. In this approach, transfer resistance values are binned and the average value of the bin and the average of the associated errors are plotted. Various models were analyzed (linear, parabolic, cubic, power law, and exponential) and a linear model of the form $\varepsilon_i = 6.8\times10^{-4} + 1.5\times10^{-3}\mathbf{d}_i$ was chosen based on having the

lowest Akaike Information Criterion (AIC) value [*Akaike*, 1974]. The AIC is a means of model selection that penalizes complex models; lower AIC values indicate better fitting models with fewer parameters.

A first-order spatial derivative smoothness-constrained inversion was performed on the first data set using R3t. This constraint is necessary to prevent unrealistic solutions to the inverse problem, but comes at the cost of smoothing out the true resistivity distribution such that sharp boundaries are less well resolved. Time-lapse data sets were adjusted prior to inversion following equation (5), and the starting model was set to the inverse result from the previous time-lapse data set to urge consistency.

Propagating error according to equation (6) assumes that errors are uncorrelated and are thus additive. This has the effect of giving time-lapse data sets larger errors than the background data set. However, in cases where systematic errors (i.e., errors from mesh discretization, forward modeling, and field configuration) dominate, as might be expected in a low electrical noise environment such as Caribou Bog, much of the error tends to cancel by the inversion approach of *Labrecque and Yang* [2001]. Although difficult to explicitly differentiate between systematic and uncorrelated errors, an initial inversion of all time-lapse data sets revealed that in the vast majority of cases starting errors exceeded the convergence criterion and the inversion could not be carried out. To address this problem, we scaled the convergence criterion by a factor of one fourth which allowed 105 of the 126 time-lapse data sets (84%) to converge successfully within two iterations. The background data set convergence criterion was not scaled and converged in six iterations.

3.5.4. Temperature Correction

After inversion of the ERI data sets, temperature correction was applied to the inverse results using the method of *Hayley et al*. [2007],

$$m_{std,j} = \left[\frac{k(T_j - 25) + 1}{k(T_{std} - 25) + 1}\right] m_j, \tag{7}$$

where $m_{std,j}$ is the voxel resistivity corrected to the standard temperature, T_j is the temperature at the location of the model voxel, T_{std} is the desired reference temperature (chosen as 25°C for this study), and k is a constant describing the linear slope coefficient between temperature and conductivity of the soil. The constant k was set as 0.0183, shown to be valid for a variety of soil types in the temperature range from 0 to 25°C [*Hayley et al*., 2007].

We used data from our HOBO temperature loggers to produce a 1-D monotonic Hermite spline function relating temperature to depth for each of the ERI data sets to allow for temperature correction of resistivity values at each voxel throughout the imaged region away from the logger locations. The monotonic Hermite spline function provides a smooth fit through discrete data while preventing overshooting and undershooting that may occur in regular cubic interpolation [*Fritsch and Carlson*, 1980]. For voxels below 6.4 m depth, the temperature was fixed to the value of the deepest sensor given that temperature is unlikely to vary significantly below this point. For example, in a 2 year study of the thermal properties of a northern peatland, *McKenzie et al*. [2007] observed less than 1°C annual variation at 4 m (the deepest point investigated in their study). Considering that each 1°C increase in temperature induces a roughly 2% decrease in resistivity, and the stated accuracy of the temperature probes used for the depth-temperature model (±0.53°C), we expect the correction to be reliable to within 1%. Although additional uncertainty exists in terms of horizontal variability in temperature (we considered a perfectly layered 1-D temperature model) and the depth-temperature model itself, these factors were beyond our means to reasonably constrain further for this study.

3.5.5. Time Series Analysis of ERI Data Sets

Each data set collected in this study consists of 47,722 voxels. To assist in the presentation of these data in an informative way, we took two approaches. The first measure we employed was to average the magnitude of the changes observed between ratio data sets in order to provide a single number to assess how much change has occurred between data sets. To do so, we calculated,

$$\overline{\rho_{rat}} = \frac{1}{M}\sum_{j=1}^{M} |m_{std,j} vol_j - 1|, \tag{8}$$

where M is the total number of model parameters (voxels) in the foreground region and vol_j is the volume of voxel j divided by the total volume of the foreground region. This is essentially the volume-weighted

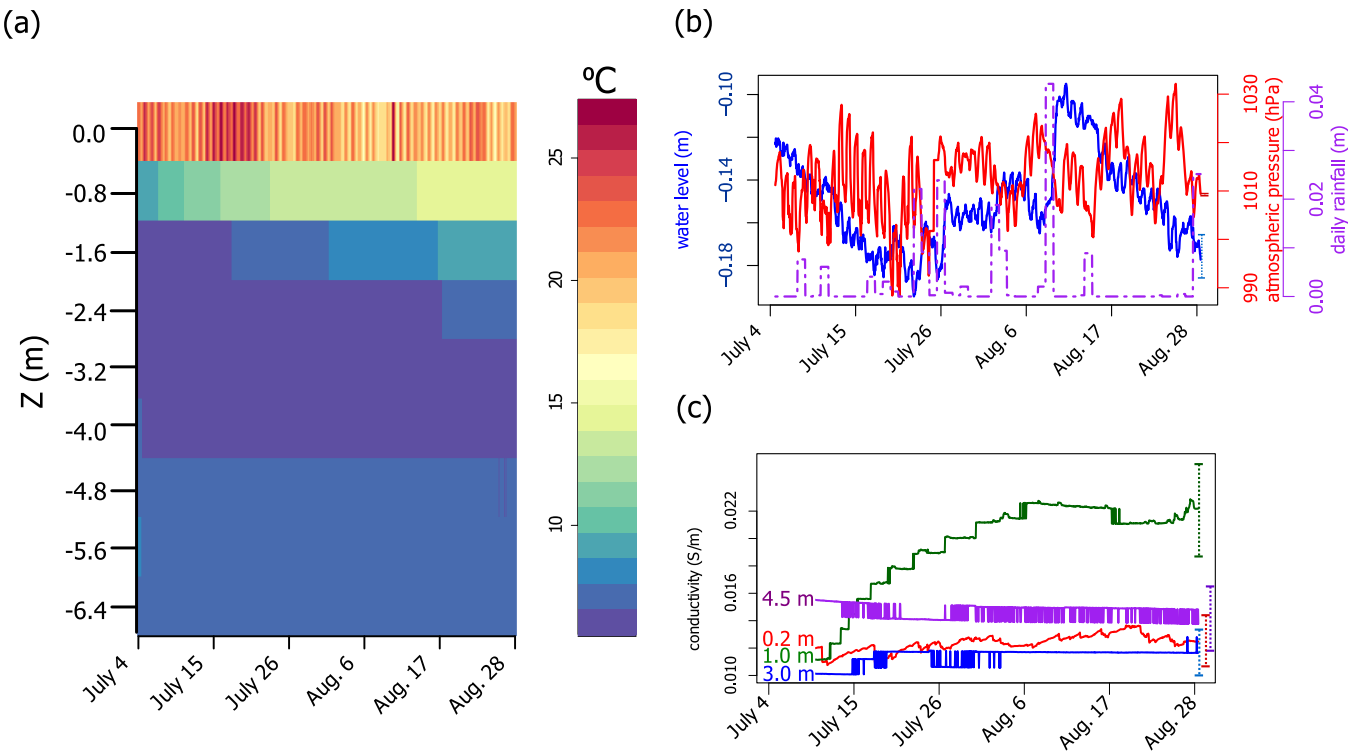

Figure 3. Plots of key environmental parameters throughout the monitoring study: (a) peat temperature recorded at the nine HOBO loggers through time; (b) water level (compensated for atmospheric pressure variations), atmospheric pressure, and rainfall events; (c) calculated pore fluid conductivity at 0.2, 1.0, 3.0, and 4.5 m.

average magnitude of ratio resistivity change, shifted to have a zero minimum. A single $\overline{\rho_{rat}}$ value is calculated for each time step, which represents the variation of resistivity in comparison to the previous measurement. All together, the ρ_{rat} values form a time series that summarize the 3-D ERI data, and therefore we can expect $\overline{\rho_{rat}}$ to reflect the overall amount of "activity" in the monitoring region since the last time step.

Our second approach was to analyze the correlation between resistivity and the measured environmental variables, i.e., atmospheric pressure, water level, and temperature. All environmental data were available at a resolution of at least 1 h, therefore we selected the datapoints most closely corresponding to each hour for our time series analysis. To make ratio resistivity inverse results directly comparable to 1 h environmental data, we used Gaussian interpolation to form intermediate data sets such that the time series for the resistivity and the environmental parameters had equal length for correlation analysis.

4. Results

4.1. Initial Site Characterization

4.1.1. Environmental Variables

Figure 3a shows variations in peat temperature throughout the study period. Diurnal variations are observed in the sensor placed just below the peat surface, ranging from 15 to 27°C. Temperatures in the region down to 2.4 m increase gradually until the end of the study period, whereas temperatures below 2.4 m range from 6 to 8°C, but remain relatively steady at each monitoring location (less than 1°C variation throughout the study period).

Water levels (Figure 3b) fluctuate between 0.1 and 0.2 m below the peat surface, being typical for a northern peatland. Although daily variations were observed (likely due to day-night shifts in evapotranspiration [*Mitsch and Gosselink*, 2007]), the water level variations mostly appear to be driven by large rainfall events. The water table generally fell from 4 July to 22 July, subsequently rose until 10 August, and then fell again until the end of the study period. Atmospheric pressure also exhibited daily variations and ranged from 990 to 1030 hPa. The month of July had a distinctly lower atmospheric pressure than August. Several relatively low-pressure events (for example, 18 July, 24 July, and 10 August; Figure 3b) occur throughout the study

and are usually accompanied by relatively large amounts of rainfall. The drops in atmospheric pressure often occur rapidly. Preceding the 18 July low, for example, the pressure dropped from 1017.8 to 1009.4 hPa over a period of 12 h.

Pore water conductivity and propagated uncertainty (based on probe accuracy, shown as dotted error bars to the right of the plot) are shown in Figure 3c. The pore water conductivity varies between 0.010 and 0.023 S m^{-1}. These values are consistent with ranges previously observed in Caribou Bog (A. S. Reeve, unpublished data, 2000). Values ranging from 0.011 to 0.014 S m^{-1} are observed in the 0.2 m depth pore water conductivity data, which we attribute to rainfall and evapotranspiration. We assume that ERI data acquired at the smallest investigation depths reflect these variations to some extent. Consequently, these investigation depths (top 0.2 m) are excluded from the time series analysis in order to focus on resistivity changes driven by FPG dynamics.

The pore water conductivity recorded at 1.0 m increased from 0.010 to 0.023 S m^{-1} in July, which is unexpected, then remained more or less steady through the rest of the study period. The July increase could result from heavy rains that occurred prior to the field campaigns and dry deposition, from solute transfer from up hydraulic gradient, or possibly due to peat mineralization and subsequent release of organic acids and other ions into the pore fluid. Another possibility could be FPG bubbles forming on the prongs of the sensors, causing instrument malfunction. Unfortunately, we have no data to support these assumptions.

The fluctuations in the 3.0 and 4.5 m data are largely due to the limited precision and accuracy of the probe measurement of bulk conductivity: the "jittering" effect results from the limits of the 0.001 S m^{-1} precision. Consequently, the pore water conductivity cannot be assumed to be entirely static. Nevertheless, without any reason to believe that there would be substantial changes in fluid conductivity at depth, we believe these data depict stable pore water conductivity, supporting our association of changes in resistivity with changes in FPG content.

Figure 4a shows the calculated sensitivity map for the first ERI background data set (4 July). As anticipated, sensitivity is highest in the foreground region of the mesh and decays toward the edges. Although all inversions were performed on the entire mesh, we henceforth only present data from the foreground region (the top 6.4 m of peat below the 28 m by 10 m electrode array). This represents an informed decision to present only those parts of the model space that likely provide reliable information on resistivity variation as inferred from the sensitivity image.

The temperature-corrected background image of the foreground region is shown in Figure 4b and depicts a relatively strong resistivity change that occurs at approximately 6.4 m, indicating the peat-mineral soil boundary and consistent with the GPR and coring data. The peat region (above 6.4 m, 24,668 voxels) has an average resistivity of 192 ohm m and standard deviation of 50 ohm m, while the mineral soil region (below 6.4 m, 174 voxels) has an average resistivity of 75 ohm m and a standard deviation of 15 ohm m. A second resistivity change is also depicted within the peat column at around 3 m (coinciding approximately with the position of the 3.45 m woody layer as per Figure 2a) characterized by a deeper region (below 3 m) with an average resistivity of 126 ohm m overlain by a shallow region (above 3 m) with an average resistivity of 161 ohm m.

Data from the VEAs were used to build further confidence in the inversion results. Since the apparent resistivity computed from the VEAs represents an average resistivity of the region surrounding the electrodes, we computed average resistivity from elements from the 3-D inversion within 1.25 m of the center of the quadripole for comparison (Figure 4c). In general, the 3-D results appear smoothed out compared to the variation observed at the VEAs, consistent with the smoothness constraint imposed by the inverse algorithm. The ERI-derived resistivities are consistently higher than the apparent resistivities from the VEAs between 2 and 5 m depth, which may result from differences in sampling volumes between the two measurements. Nevertheless, a consistent pattern is visible between the ERI and VEA results, adding confidence that the time-lapse ERI inversions are reliable throughout the part of the model domain defined to have sufficient resolution.

4.2. Monitoring of Resistivity Changes

4.2.1. Time-Lapse ERI Results and Atmospheric Pressure

Figure 5a shows $\overline{\rho_{rat}}$ and ratio changes in atmospheric pressure. Figures 5b–5f show the actual ERI ratio resistivity values from points along the time series, while Figure 6 shows increases and decreases in ratio

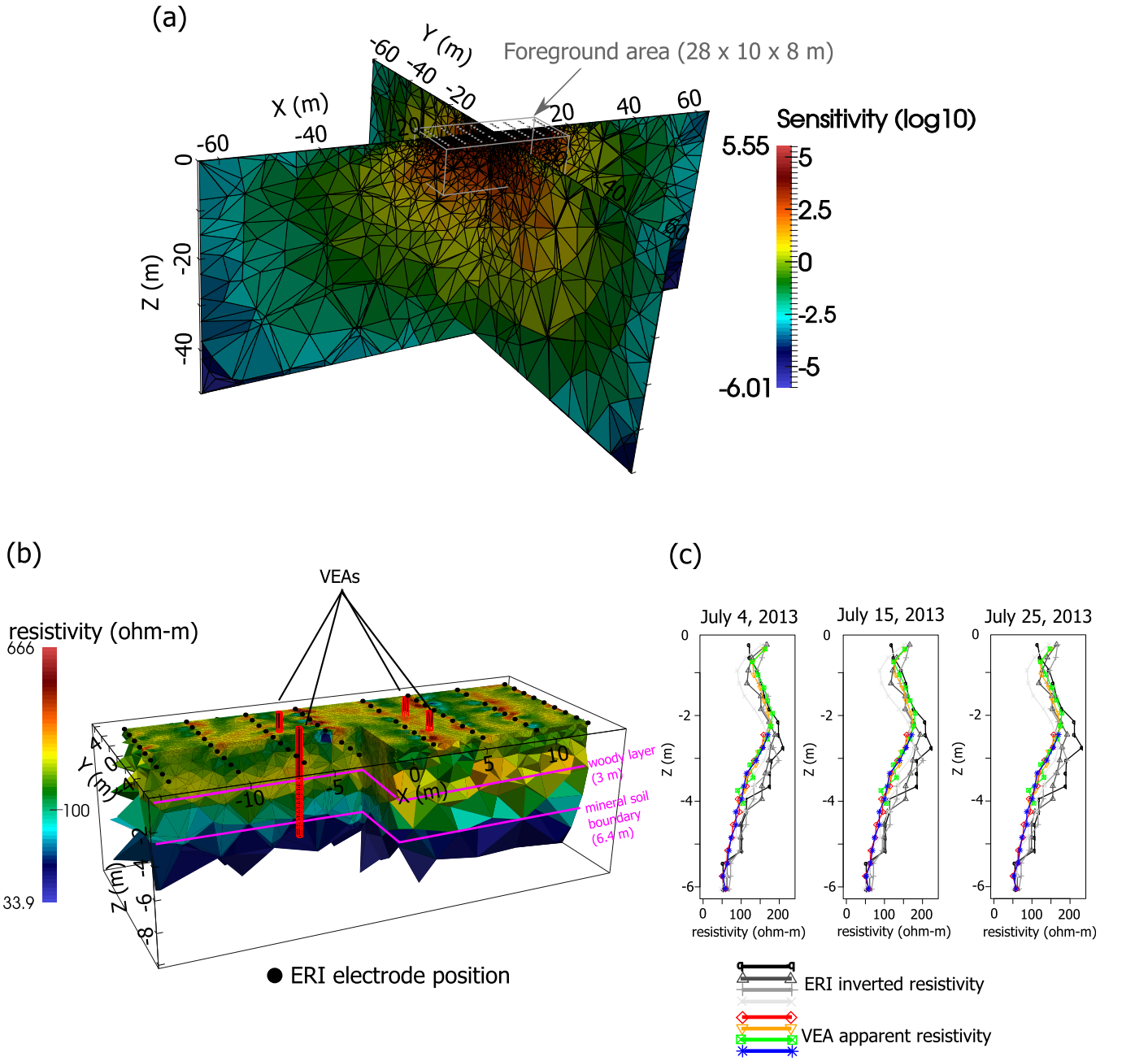

Figure 4. Results of the background data set inversion from 4 July. (a) Fence diagram showing sensitivity of voxels within the FEM mesh—the expected pattern of decaying sensitivity away from the electrodes is observed; (b) cut of the inverted 3-D background data set. The inverted resistivity values depict a boundary near the base of the peat and at a woody layer (shown as pink lines); (c) apparent resistivity values captured by the vertical electrode arrays compared with the inverted resistivity values from the voxels corresponding to the vertical electrode array measurement locations. The values from the 3-D inversion are smoothed, but show good agreement with the vertical electrode arrays in terms of magnitude and shape.

resistivity for a selected time period centered on 6 July (Figure 5b). The distribution of ρ_{rat} is leptokurtic (kurtosis $\gg$ 0) with a mean slightly less than 1 (0.99996), a standard deviation of 0.002, and bounds of 0.868 and 1.14. We used the standard deviation to apply a threshold to the ERI images in Figures 5b–5f to only show absolute changes greater than 0.2% between the 1 h interpolated data sets. Ratio resistivity values smaller than 0.9 or larger than 1.1 are shown as color saturated.

Visually, $\overline{\rho_{rat}}$ appears to give a good indication of the overall ratio changes occurring in the actual ERI images (see movie ms1 in supporting information to view an animation of all time-lapse ERI images). Figures 5b–5d and 5f correspond to the four largest $\overline{\rho_{rat}}$ events and occur during abrupt drops in

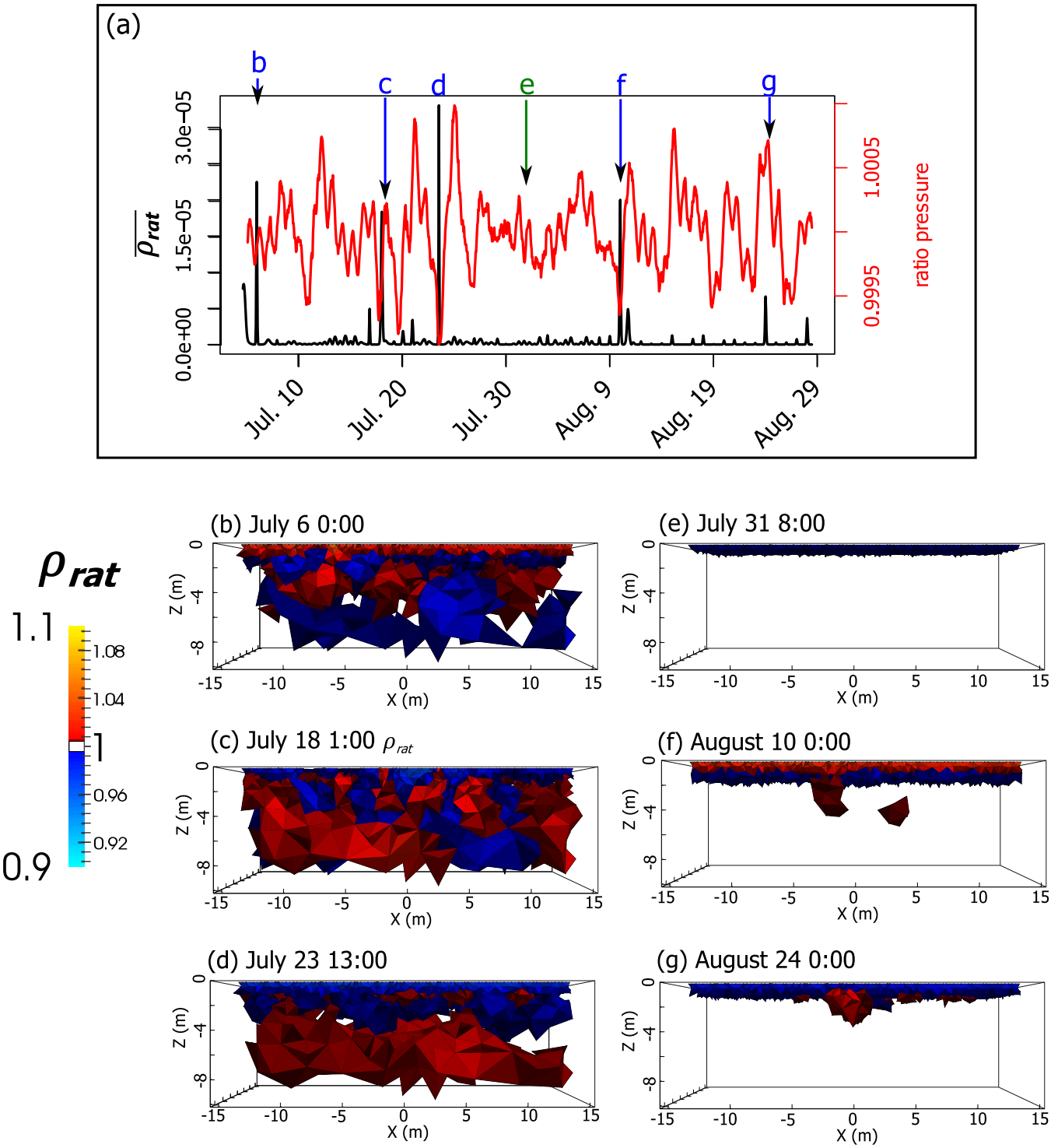

Figure 5. Time-lapse ERI results: (a) average absolute ratio resistivity magnitude ($\overline{\rho_{rat}}$, black) plotted with ratio atmospheric pressure (red). (b–g) select ratio ERI images from the time series. A threshold has been applied to only show changes with magnitude > 0.002 to enhance visibility.

atmospheric pressure (low ratio pressure), whereas Figure 5g is a relatively large $\overline{\rho_{rat}}$ event occurring during a period of rising atmospheric pressure, but closely follows a drop in atmospheric pressure (within 24 h). Figure 5e is a representative image for a relatively static time both in terms of $\overline{\rho_{rat}}$ and atmospheric pressure. Each of the images in Figures 5a–5g shows ratio resistivity changes greater than 0.2% across the

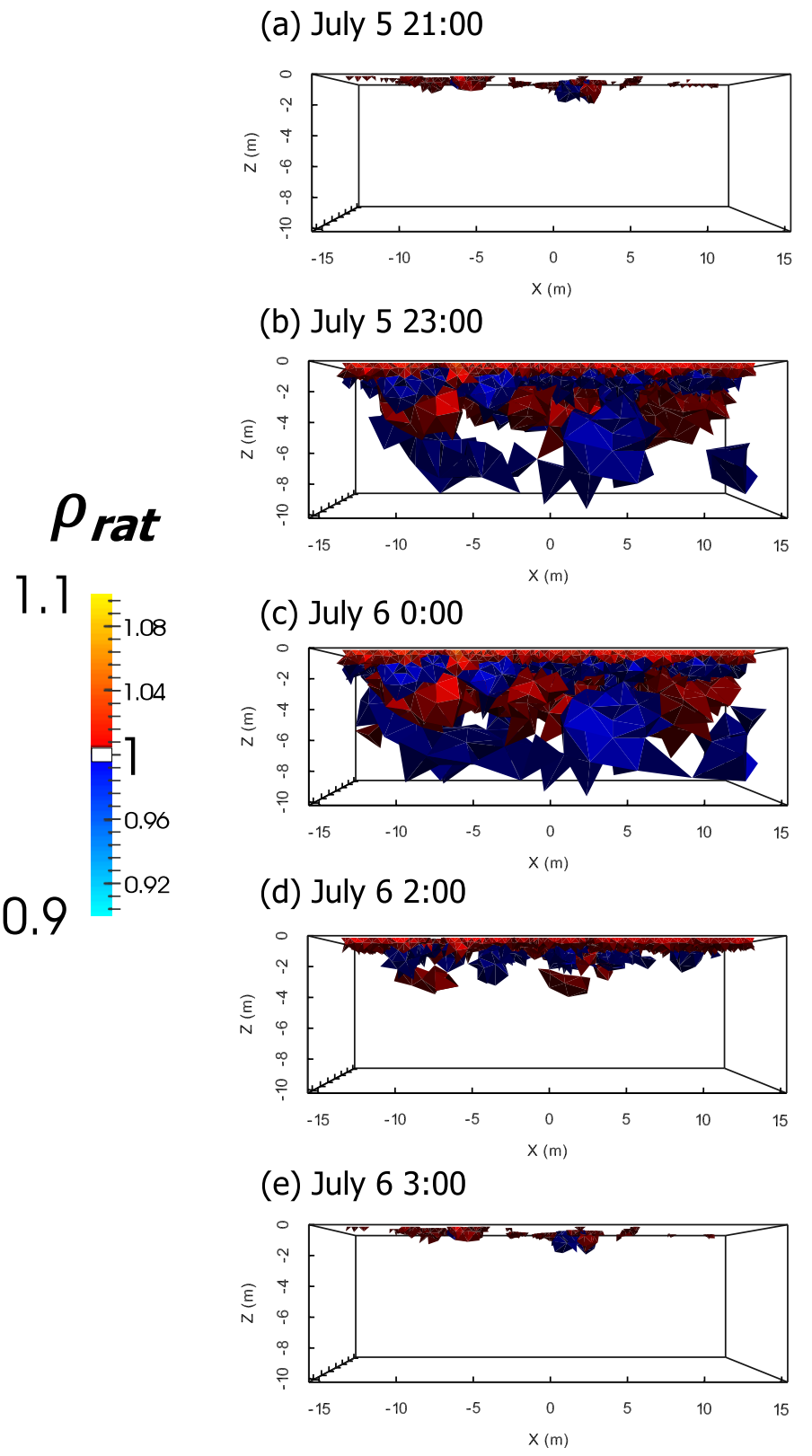

Figure 6. Selected time-lapse images (a and b) before, (c) during, and (d and e) following the 6 July $\overline{\rho_{rat}}$ event.

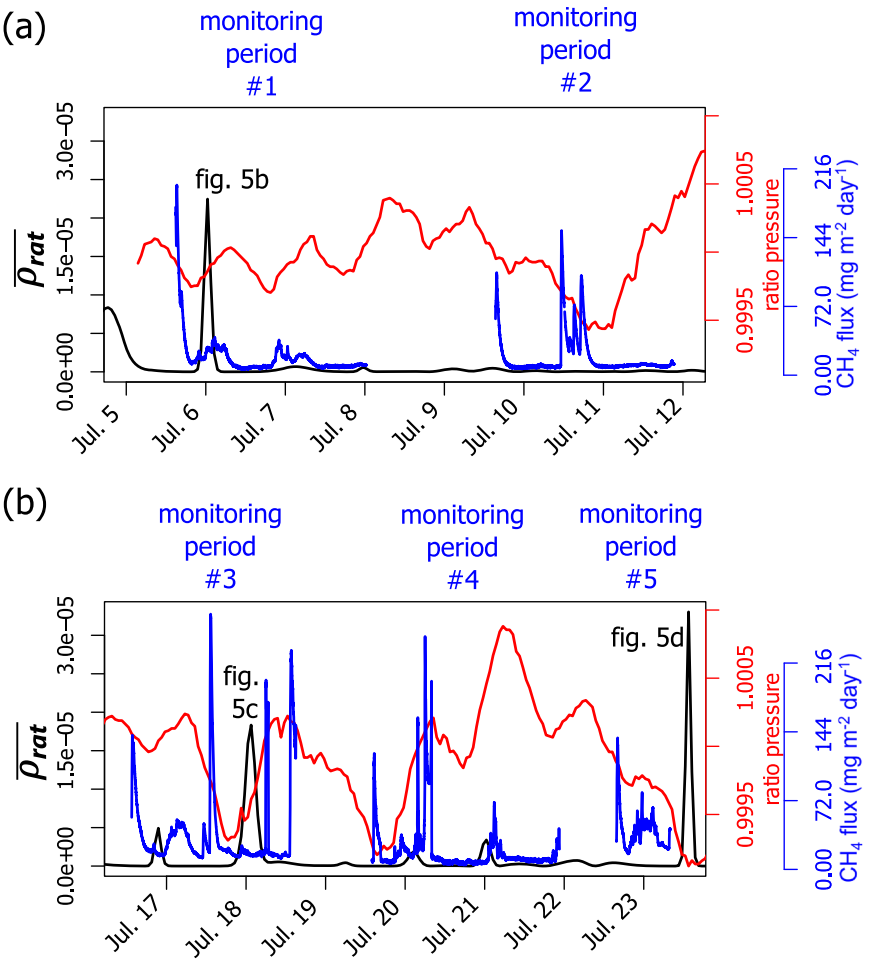

Figure 7. Data from the five dynamic flux chamber monitoring periods (blue), the average absolute ratio resistivity magnitude ($\overline{\rho_{rat}}$, black), and ratio atmospheric pressure (red).

shallow peat layer, while the 3 July data sets corresponding to large $\overline{\rho_{rat}}$ events (Figures 5b–5d) depict strong ratio resistivity changes at depth. Figure 5b depicts predominantly decreases in ratio resistivity in the shallow peat and predominantly increases in the deep peat, while Figures 5c and 6d show the reverse pattern.

The August images (Figures 5f and 5g) show fewer ratio resistivity changes greater than the 0.2% threshold than the July images (Figures 5b–5d), but depict a similar pattern to that observed in Figures 5c and 5d. In Figures 5f and 5g, changes in $\rho_{rat} > 0.2\%$ are limited to the uppermost layer and a region of increase in the center of the image not extending beyond 4 m depth. The average ratio resistivity for 10 August midnight (corresponding to Figure 5f) is positive, while the average ratio resistivity for 24 August midnight (corresponding to Figure 5g) is negative, despite the positive anomaly observed in the center of the image. Additional plots showing depth slices of Figures 5b–5d, 5f, and 5g as well as average ratio resistivity values from various depths along the time series are shown in the supporting information, but are not included here for brevity.

4.2.2. Direct Flux Measurements, Water Levels, and Atmospheric Pressure Compared to ERI

Figure 7 shows ratio of atmospheric pressure magnitude, $\overline{\rho_{rat}}$, and CH_4 flux data from the dynamic flux chamber during five monitoring periods. The flux data consist of a steady, background flux (<15 mg CH_4 m^{-2} d^{-1}) punctuated by relatively large flux events that show up as spikes (up to 260 mg CH_4 m^{-2} d^{-1}). These spikes occur mostly during periods of decreasing atmospheric pressure (as in flux monitoring periods 1, 2, 5, and partly in 3), but also appear to occur during rising atmospheric pressure (flux monitoring periods 4 and partly in 3). The largest $\overline{\rho_{rat}}$ events are annotated with their corresponding images in Figure 5.

There is some correspondence between CH_4 flux recorded at the center of the array and $\overline{\rho_{rat}}$, in that elevated flux apparently corresponds to elevated $\overline{\rho_{rat}}$ on several occasions (Figure 7). Flux monitoring periods

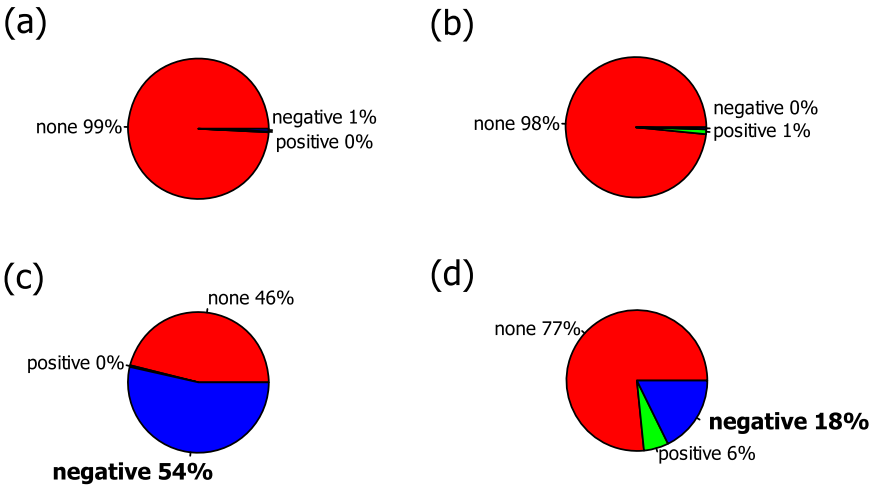

Figure 8. Pie charts summarizing the Pearson correlation coefficient between ERI resistivity and environmental variables for deep (> 1 m) and shallow (top meter) peat. Note only "moderate" to "strong" correlations (larger than ±0.4) are shown. (a and b) Correlations between resistivity and atmospheric pressure; 99% of the (a) shallow and (b) deep peat regions show little to no linear correlation. (c and d) Correlations between resistivity and water levels; over half the shallow peat region. Figure 8c shows moderate to strong negative correlations with water level, while most of the deep peat region (Figure 8d) shows no moderate to strong linear relationship with water level, 18% of the region still exhibits a negative correlation.

1, 3, and 4 depict this general visual relationship, although there appears to be little correlation with the direct flux measurements and $\overline{\rho_{rat}}$ in terms of magnitude. Additionally, monitoring period 2 shows little change in $\overline{\rho_{rat}}$ despite collection of several ERI data sets during this time period and a drop in atmospheric pressure and corresponding elevated CH_4 flux recorded at the surface. There are no large $\overline{\rho_{rat}}$ events during monitoring period 5, but there is a large event that occurs a few hours later during an atmospheric pressure minimum (the CH_4 flux monitoring time series does not overlap this event).

Figures 8a and 8b show the percentage of the peat volume with moderate to strong (magnitude of $r > 0.4$) linear correlations between ERI resistivity and atmospheric pressure in the shallow and deep peat. Almost no linear correlation exists between atmospheric pressure and resistivity at either depth, even if there appears to be a time lag of various lengths between drops in atmospheric pressure and spikes in $\overline{\rho_{rat}}$ (Figure 5a). In contrast, Figures 8c and 8d show correlations between water levels and resistivity in the shallow and deep peat. In both cases, a significant portion of the peat volume exhibits moderate to strong negative linear correlations (54% in the shallow peat, 18% in the deep peat). Figure 9a shows only voxels with correlations of magnitude greater than 0.7, and Figure 9b shows an example time series plot of resistivity and water levels. These correlations occur in the region below the water table, which varies throughout the study period between 0.1 and 0.2 m depth (Figure 9a).

5. Discussion

5.1. The Unique Nature of ERI Measurements: Monitoring FPG Dynamics in Peat Soils at Different Temporal Scales

This study shows the potential of ERI to monitor biogenic gas dynamics within peat soils at high (i.e., hourly) temporal scales. Despite that the technique represents an indirect measurement of gas content as based on changes in electrical conductivity, the method is unique for its ability to autonomously monitor gas dynamics within the peat matrix, therefore representing a minimally invasive measurement. Although installation of the VEAs represent greater disturbance to the peat (compared to the surface ERI), the results of this study indicate that surface array measurements are sensitive enough to observe FPG dynamics in peat, and that within peat VEA measurements are likely not required for future studies of this kind. Furthermore, the ERI method is able to provide information on gas dynamics and migration through the peat column beyond traditional methods (i.e., chambers) that are only able to capture gas releases once reaching the peat-air interface. For example, Figure 6 shows increases and decreases in ratio resistivity within the shallow and deep layer around the drop in atmospheric pressure on 6 July. The changes are interpreted as gas content

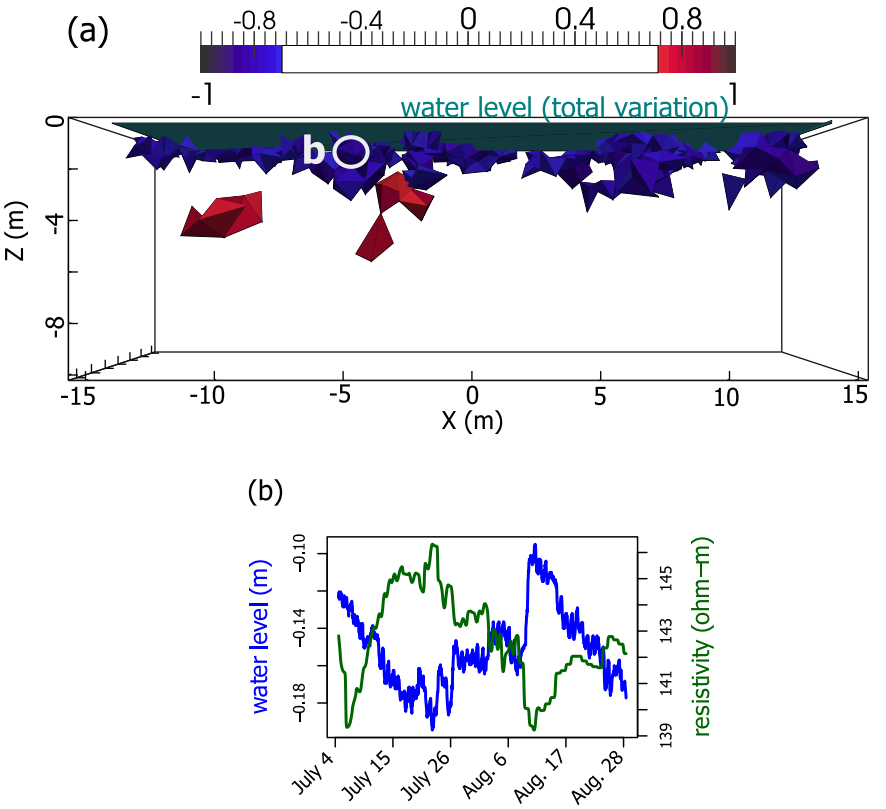

Figure 9. Correlation between water level and resistivity; (a) voxels with correlation coefficients having magnitudes greater than 0.7. The range of water levels are also shown; (b) water level (blue) and resistivity (green) time series at a voxel in the shallow peat exhibiting a −0.89 correlation.

increasing in the shallow layer while decreasing in the deeper layer. This pattern might represent vertical migration of gas from deeper to shallower layers. Being able to capture such trends in gas dynamics within the peat column at the temporal resolution shown here (i.e., hourly) has never, to our knowledge, been reported before and exemplifies the unique potential of ERI to monitor gas dynamics in peat soils.

We note that there are some inherent limitations to interpretation of time-lapse ERI as a proxy for FPG dynamics. For one, ERI measurements take time to perform (in this study, 1.25 h), and thus limit the temporal resolution. Inverted ratio resistivity values represent the sum of all resistivity changes between data sets, which may reflect multiple FPG events. Second, given the time it takes for ERI data collection to occur, ERI measurements do not capture an instantaneous time slice of a dynamic process. Although we are treating changes in resistivity as having occurred between two data sets, such changes could partially represent changes that are taking place during data collection.

Given the indirect nature of ERI measurements, changes in resistivity have multiple interpretations. We have asserted that increases in total FPG volume will be mirrored as increases in resistivity; likewise decreases in FPG volume will show as decreases in resistivity. Volume changes in FPG result from two main processes. First, abrupt gas transfer and/or ebullition events will result in substantial local gains or losses in FPG content, and should be visible in ERI images assuming the events are of detectable magnitude. Second, pressure variations (due to atmospheric or hydrostatic fluctuations) will result in volume changes to the FPG bubbles themselves according to Henry's Law and the ideal gas law. Decreases in pressure allow bubbles to expand, while increases in pressure cause bubble contraction. Significant dilation of FPG bubbles should appear as an increase in resistivity and *vice versa*.

For example, a decrease in water level of 10 cm (the approximate range observed in this study, see Figure 3) is roughly equivalent to a decrease in hydrostatic pressure of 10 hPa below the water table. According to Henry's Law and the Ideal Gas law and assuming an average temperature of 10°C, an ambient pressure of

1000 hPa and that the FPG consists solely of methane, this change would induce an approximate +1% increase in bubble volume. Assuming a porosity representative of Caribou Bog of 0.94 [*Parsekian et al*., 2012] and employing equation (3), this would be manifested as a +1.5% increase in ratio resistivity. This change is much greater than the average data error observed (0.46%), and should be well within detection limits of our ERI setup.

Although a quantitative link directly mapping ERI data to FPG content has been deemed unreasonable (in our study as well as the laboratory studies of *Slater et al*. [2007] and *Kettridge et al*. [2011]), we have taken careful measures to ensure that ERI inversion results can be qualitatively interpreted as changes in FPG content. First, we compensated for temperature in the ERI inverse results using data from eight sensors spanning from the peat surface to the mineral soil (Figure 3a). Second, we observed stable pore fluid conductivity values at 0.2, 3.0, and 4.5 m depth, although the 1.0 m conductivity probe did exhibit some variation (Figure 3c). Third, we confine our interpretations to below the water table (maximum depth 0.2 m, Figure 3b) to avoid mistakenly interpreting water level variation as gas development/release. Fourth, we constrain our analysis to the foreground (high sensitivity) region of the ERI inversion mesh (Figure 4a). Fifth, we cross validated our ERI inverse resistivity magnitudes with apparent resistivity recorded at the VEAs (Figure 4c). Finally, a synthetic study suggests that changes in FPG content of the magnitude we would expect to see in Caribou Bog are detectable using ERI (see supporting information).

The ERI difference inversion successfully captured several major events within the peat during the 2 month study period. Rates of resistivity change of over 0.2% per hour were observed throughout the entire peat column during these events. Such events also seem to indicate some general trends in biogenic gas accumulation and release during the 2 month monitoring period that may be potentially related to the stratigraphy of the peat column. For example, the event on 6 July (Figure 5b) shows a marked decrease in resistivity below 3 m coinciding with an increase above 3 m that could be interpreted as a breach in the wooden layers described between 3 and 4 m (Figure 2) followed by release of gas that moves into the layers above. Subsequent events (i.e., 18 and 23 July, Figures 5c and 5d, respectively) show a marked increase in resistivity below 3 m that could be interpreted as periods where gas accumulation below the wooden layer increases gradually due to entrapment.

Comparison of the ERI data with the CH_4 flux data and the atmospheric pressure variations (Figure 7) suggests that the large $\overline{\rho_{rat}}$ events represent either large-scale ebullition and/or FPG transfer events, FPG bubble volume changes due to changes in pressure, or both. Each of these events (Figures 5b–5d, 5f, and 5g) occurs during or soon after a rapid drop in atmospheric pressure (Figure 5a). The events shown in Figures 5d, 5c, and 5f occur within 4 h of the first, second, and fourth largest local minima in ratio atmospheric pressure, whereas Figures 5b and 5g occur within several hours of smaller local ratio atmospheric pressure minima. These abrupt changes in FPG content associated with sudden drops in atmospheric pressure are consistent with the findings of many others [*Bon et al*., 2014; *Comas et al*., 2011a; *Kellner et al*., 2006; *Kettridge et al*., 2011; *Tokida et al*., 2007; *Waddington et al*., 2009; *Yu et al*., 2014].

Most of the events shown in Figures 5c, 5d, 5f, and 5g depict a pattern of decreased ρ_{rat} in the surface layer while increases primarily occur below 1 m depth. This resistivity structure is consistent with ebullition primarily occurring from the shallow peat (decreasing resistivity), and gas bubble expansion (increasing resistivity) due to decreasing atmospheric pressure occurring in the deep peat. Figures 5f and 5g show a localized increase in ρ_{rat} in the deep peat near the center of the study area. This region of increased ρ_{rat} may reflect a gas pocket formed from the upward migration and subsequent expansion of many small bubbles within this pocket due to decreased atmospheric pressure. Although this localized increase occurs in the center of the ERI array where sensitivity is relatively greater, it is unlikely that this region is simply an artifact of the ERI sensitivity given that both our synthetic and field tests were able to image large (>0.2%) changes in resistivity outside of this area.

Overall, the patterns observed in this time-lapse resistivity data set support the shallow peat model of *Coulthard et al*. [2009] in that ebullition appears to most commonly originate from the shallow (upper meter) peat rather than the deep peat (see movie ms1 in supporting information). As we emphasize, the link between resistivity data and FPG content is not sufficiently robust to provide an estimate of the actual volumes of gas being released from either zone. Therefore, although unlikely based on our data, it is possible that the deep peat ebullition event observed in Figure 5b may be responsible for significantly more FPG

release than the other events we observe. In addition, we note that this study took place in the summer months and that gas dynamics vary seasonally [*Comas et al*., 2008]. For example, the deep peat may play a larger role during the fall and winter months as surface temperatures cool and the shallow peat eventually freezes.

5.2. Comparison of ERI and Direct Flux Data

Figures 5b–5d and 5f show the four largest events in terms of $\overline{\rho_{rat}}$. Of these events, only the smallest, Figure 5f, fails to show >0.2% per hour changes throughout the entire peat profile, although large resistivity changes are still observed in the upper layer. Although there is some correspondence between CH_4 flux recorded at the center of the array and $\overline{\rho_{rat}}$, there is no clear (i.e., quantitative) relationship between the timing and magnitude of these two parameters. These observations highlight the difference in scale between ERI measurements and chamber-based measurements. Apparently, large ebullition events recorded at the CH_4 flux chamber do not necessarily appear as large events throughout the peat volume sampled by ERI. Clearly, the spatiotemporal resolution of the ERI is not fine enough to capture such spatially localized events recorded at the flux chamber. Such discrepancies illustrate how upscaling from chamber measurements to a global scale could potentially be very misleading, and finding the "appropriate" spatiotemporal scale to capture FPG dynamics in wetlands is an ongoing research problem as illustrated in other recent studies [for example, *Stamp et al*., 2013; *Comas and Wright*, 2014].

5.3. Time Series Analysis of ERI, Water Levels, and Atmospheric Pressure

Atmospheric pressure and resistivity exhibit almost no linear correlation in either shallow or deep zones (Figures 8a and 8b). This may be due to conflicting effects of atmospheric pressure on FPG dynamics: low pressure driving both gas expansion and ebullition, high pressure both causing bubble contraction and enhancing mobility (allowing for transfer/release). Although abrupt pressure decreases clearly trigger large changes in resistivity, particularly at depth, there is no linear dependency of resistivity on pressure. This indicates that the nonstationary dependency of the peat gas dynamics on episodic changes in atmospheric pressure only.

A substantial portion of the peat volume shows moderate to strong linear correlations with water levels (Figures 8c and 8d). Figure 9b illustrates that the strong negative correlations are primarily trend driven, as the resistivity does not appear to respond to the small fluctuations in water level. This is confirmed by differencing the two time series, which reveals weak to no correlation (not shown). Although each data set was interpolated to a common 1 h interval for time series analysis, it is possible the small fluctuations in water level are not reflected in the ERI data due to differences in the actual sampling rate of the instruments. The water level data were sampled at 15 min intervals, whereas ERI data were collected no faster than 2 h apart.

We therefore attribute the moderate to strong negative correlations between resistivity and water level below 0.2 m depth to bubble contraction/dilation due to hydrostatic pressure variation. The fact that more correlation is observed in the shallow peat may have to do with (1) the enhanced sensitivity of ERI within this region, (2) possibly higher FPG content in the shallow peat, and/or (3) a greater ability for bubbles to expand/constrict in the shallow peat possibly due to generally higher elasticity of the shallow peat matrix.

Assuming the FPG release dynamics we observe are primarily driven by pressure variations, we might expect to see similar relationships between resistivity and water level as well as resistivity and atmospheric pressure. We attribute this discrepancy to the magnitude of hydrostatic pressure variations, equivalent to roughly 10 hPa over weeks, versus atmospheric pressure, which varies up to 20 hPa in a single day. Thus, it seems that atmospheric pressure is primarily responsible for driving large FPG transfer and release events, whereas hydrostatic pressure may also contribute to these events (the events observed in Figures 5c and 5d also occur during relatively low water levels). Whereas abrupt changes in atmospheric pressure episodically trigger major gas releases, water levels appear to immediately change bubble size through compression and expansion. This phenomenon was clearly observed (visually and through GPR monitoring) by *Chen and Slater* [2015] in a peat monolith taken from Caribou Bog.

6. Conclusions

ERI is a unique method for autonomously monitoring FPG dynamics in peat soils at high (i.e., hourly) temporal scales. The method is able to provide information on gas dynamics and migration through the peat

column while bringing some insights about mechanisms for FPG releases. For example, drops in atmospheric pressure appear to exert control over FPG transfer and ebullition events as inferred from ERI. Most of these events are associated with a loss of FPG in the shallow peat and an increase in FPG in the deep peat; however, we were unable to establish a quantitative link between atmospheric pressure and FPG content using our ERI data. The increase in FPG content in the deep peat during drops in atmospheric pressure may result from collection of gas below a confining layer and/or bubble expansion during low pressure. In one notable case, we observed a large decrease in FPG content from the deep peat. This likely reflects a rupturing event in which FPG buildup in the deep peat breaks through a confining layer and transfers to the shallow peat and/or is released to the atmosphere.

Water level variations were not found to trigger ebullition or FPG transfer events in this study. However, even small variations in hydrostatic pressure (less than 10 hPa over the 2 month study period) appear to control FPG bubble contraction/dilation, as evidenced by the substantial portion of the shallow and deep peat showing moderate to strong negative linear correlation between water levels and resistivity. Although it is probable that water level variation could trigger ebullition and gas transfer in a manner similar to atmospheric pressure, the gradual nature of the hydrostatic pressure change compared to atmospheric pressure change makes this hydrostatic pressure trigger less likely. Likewise, given the relatively abrupt rate of atmospheric pressure change ($>$20 hPa in a single day), the temporal resolution of our ERI measurements (collected twice a day on average) may not be sufficient to capture rapid changes in bubble volume.

Although power considerations and data collection time limited our maximum temporal resolution, this is not a limitation of the ERI technique. Depending on the data collection scheme, time-lapse ERI data could be collected every few minutes or possibly even more rapidly. In addition, we have shown the ability of time-lapse ERI for depicting an in situ dynamic process occurring over several meters within the deep peat (down to 6.4 m), a regime otherwise difficult to sample. Importantly, ERI also minimizes disturbance of peat structure. Although we recognize the inability of the technique to directly estimate FPG content, there is immense value in employing ERI coupled with other environmental measurements to study biogenic gas dynamics in wetland soils. In the future, ERI could be used to directly compare below ground CH_4 dynamics with CH_4 fluxes at the surface if coupled with systems that measure on similar scales (such as infrared CH_4 cameras [*Gålfalk et al*., 2015] and/or multiple chambers [*Stamp et al*., 2013]). Such a study would serve to constrain conceptual models of below ground peatland gas dynamics and further clarify the relative importance of shallow versus deep peat to methane fluxes.

Acknowledgments
We would like to thank William Wright for providing geospatial data and for all his help in the field, the field assistants in the 2013 Caribou Bog research campaign (Jonathan Algeo, Zachary Freeburg, Barbara Goldman, Adriana Morocho, and Kisa Mwakanyamale), and Gordon Osterman and Xi Chen for their assistance in removing ERI equipment. We would also thank Andrew Parsekian for remotely troubleshooting GPR issues, Jay Nolan for his advice on setting up the autonomous ERI array, Andrew Binley for assisting with R3t, and Judy Robinson for her advice in developing unstructured meshes. This material is based on the work supported by the National Science Foundation under grant 1045084. All data are available from the first author (neil.terry@rutgers.edu).

References

Akaike, H. (1974), A new look at the statistical model identification, *IEEE Trans. Autom. Control*, *19*, 716–723.
Baird, A. J., C. W. Beckwith, S. Waldron, and J. M. Waddington (2004), Ebullition of methane-containing gas bubbles from near-surface *Sphagnum* peat, *Geophys. Res. Lett.*, *31*, L21505, doi:10.1029/2004GL021157.
Beckwith, C. W., and A. J. Baird (2001), Effect of biogenic gas bubbles on water flow through poorly decomposed blanket peat, *Water Resour. Res.*, *37*, 551–558.
Binley, A., and A. Kemna (2005), Electrical Methods, in *Hydrogeophysics, Water Science and Technology Library*, vol. 50, edited by Y. Rubin and S. S. Hubbard, pp. 129–156, Springer, Dordrecht, Netherlands, doi:10.1007/1-4020-3102-5.
Binley, A., P. Winship, L. J. West, M. Pokar, and R. Middleton (2002), Seasonal variation of moisture content in unsaturated sandstone inferred from borehole radar and resistivity profiles, *J. Hydrol.*, *267*, 160–172, doi:10.1016/S0022-1694(02)00147-6.
Bloom, A. L. (1963), Late-Pleistocene fluctuations of sealevel and postglacial crustal rebound in coastal maine, *Am. J. Sci.*, *261*(9), 862–879, doi:10.2475/ajs.261.9.862.
Bon, C. E., A. S. Reeve, L. Slater, and X. Comas (2014), Using hydrologic measurements to investigate free-phase gas ebullition in a Maine peatland, USA, *Hydrol. Earth Syst. Sci.*, *18*, 953–965, doi:10.5194/hess-18-953-2014.
Bridgham, S. D., H. Cadillo-Quiroz, J. K. Keller, and Q. Zhuang (2013), Methane emissions from wetlands: Biogeochemical, microbial, and modeling perspectives from local to global scales, *Global Change Biol.*, *19*(5), 1325–1346.
Chanton, J. P., J. Bauer, P. H. Glaser, D. I. Siegel, C. Kelley, S. C. Tyler, E. A. Romanowicz, and A. Lazrus (1995), Radiocarbon evidence for the substrates supporting methane formation within northern Minnesota peatlands, *Geochim. Cosmochim. Acta*, *59*, 3663–3688.
Chasar, L. C. (2002), Implications of environmental change for energy flow through natural systems: Wetlands and coastal systems, PhD dissertation, Dep. of Oceanogr., Fla. State Univ., Tallahassee.
Chasar, L. S., J. P. Chanton, P. H. Glaser, D. I. Siegel, and J. S. Rivers (2000a), Radiocarbon and stable carbon isotopic evidence for transport and transformation of dissolved organic carbon, dissolved inorganic carbon, and CH_4 in a northern Minnesota peatland, *Global Biogeochem. Cycles*, *14*, 1095–1108.
Chasar, L. S., J. P. Chanton, P. H. Glaser, and D. I. Siegel (2000b), Methane concentration and stable isotope distribution as evidence of rhizospheric processes: Comparison of a fen and bog in the Glacial Lake Agassiz peatland complex, *Ann. Bot.*, *86*, 655–663.
Chen, X., and L. Slater (2015), Gas bubble transport and emissions for shallow peat from a northern peatland: The role of pressure changes and peat structure, *Water Resour. Res.*, *51*, 151–168, doi:10.1002/2014WR016268.
Cheng, S.-W., T. K. Dey, H. Edelsbrunner, M. A. Facello, and S.-H. Teng (1999), Sliver exudation, in *Proceedings of the Fifteenth Annual Symposium on Computational Geometry*, pp. 1–13, ACM, N. Y., doi:10.1145/304893.304894.

Christensen, T. R., A. Ekberg, L. Ström, M. Mastepanov, N. Panikov, M. Öquist, B. H. Svensson, H. Nykänen, P. J. Martikainen, and H. Oskarsson (2003), Factors controlling large scale variations in methane emissions from wetlands, *Geophys. Res. Lett.*, *30*(7), 1414, doi:10.1029/2002GL016848.

Comas, X., and L. Slater (2004), Low-frequency electrical properties of peat, *Water Resour. Res.*, *40*, W12414, doi:10.1029/2004WR003534.

Comas, X., and L. Slater (2007), Evolution of biogenic gases in peat blocks inferred from noninvasive dielectric permittivity measurements, *Water Resour. Res.*, *43*, W05424, doi:10.1029/2006WR005562.

Comas, X., and W. Wright (2014), Investigating carbon flux variability in subtropical peat soils of the Everglades using hydrogeophysical methods, *J. Geophys. Res. Biogeosci.*, *119*, 1506–1519, doi:10.1002/2013JG002601.

Comas, X., L. Slater, and A. Reeve (2005), Spatial variability in biogenic gas accumulations in peat soils is revealed by ground penetrating radar (GPR), *Geophys. Res. Lett.*, *32*, L08401, doi:10.1029/2004GL022297.

Comas, X., L. Slater, and A. Reeve (2008), Seasonal geophysical monitoring of biogenic gases in a northern peatland: Implications for temporal and spatial variability in free phase gas production rates, *J. Geophys. Res.*, *113*, G01012, doi:10.1029/2007JG000575.

Comas, X., L. D. Slater, and A. S. Reeve (2011a), Atmospheric pressure drives changes in the vertical distribution of biogenic free-phase gasses in a northern peatland, *J. Geophys. Res.*, *116*, G04014, doi:10.1029/2011JG001701.

Comas, X., L. D. Slater, and A. S. Reeve (2011b), Pool patterning in a northern peatland: Geophysical evidence for the role of postglacial landforms, *J. Hydrol.*, *399*(3-4), 173–184, doi:10.1016/j.jhydrol.2010.12.031.

Coulthard, T., A. J. Baird, J. Ramirez, and J. M. Waddington (2009), Methane dynamics in peat: The importance of shallow peats and a novel reduced-complexity approach for modeling ebullition, in *Carbon Cycling in Northern Peatlands*, edited by A. J. Baird et al., 299 pp., AGU, Washington, D. C.

Crill, P. M., K. B. Bartlett, R. C. Harriss, E. Gorham, E. S. Verry, D. I. Sebacher, L. Madzar, and W. Sanner (1988), Methane flux from Minnesota peatlands, *Global Biogeochem. Cycles*, *2*, 371–384.

Crill, P. M., K. B. Bartlett, and N. T. Roulet (1992), Methane flux from boreal peatlands, *Suo*, *43*, 173–182.

Daily, W., A. Ramirez, and A. Binley (2004), Remote monitoring of leaks in storage tanks using electrical resistance tomography: Application at the Hanford Site, *J. Environ. Eng. Geophys.*, *9*, 11–24.

Davis, R. B., and D. S. Anderson (1999), A numerical method and supporting database for evaluation of Maine peatlands as candidate natural areas, *Tech. Bull. 175*, 166 pp., Univ. of Maine, Maine Agric. and For. Exp. Stn., Orono.

Dunfield, P., K. Knowles, R. Dumont, and T. Moore (1993), Methane production and consumption in temperate and subarctic peat soils: Response to temperature and pH, *Soil Biol. Biochem.*, *25*, 321–326.

Forster, P., et al. (2007), Changes in atmospheric constituents and in radiative forcing, in *Climate Change 2007: The Physical Science Basis, Contribution of Working Group I to the Fourth Assessment Report of the Intergovernmental Panel on Climate Change*, edited by S. Solomon et al., pp. 131–234, Cambridge Univ. Press, Cambridge, U. K.

Fritsch, F. N., and R. E. Carlson (1980), Monotone piecewise cubic interpolation, *SIAM J. Numer. Anal.*, *17*, 238–246.

Gålfalk, M., G. Olofsson, P. Crill, *and* D. Bastviken (2015), Making methane visible, *Nat. Clim. Change*, *6*, 426–430, doi:10.1038/nclimate2877.

Geuzaine, C., and J. F. Remacle (2009), Gmsh: A 3-D finite element mesh generator with built-in pre- and post- processing facilities, *Int. J. Numer. Methods Eng.*, *79*(11), 1309–1331, doi:10.1002/nme.2579.

Glaser, P. H., J. P. Chanton, P. Morin, D. O. Rosenberry, D. I. Siegel, O. Ruud, L. I. Chasar, and A. S. Reeve (2004), Surface deformations as indicators of deep ebullition fluxes in a large northern peatland, *Global Biogeochem. Cycles*, *18*, GB1003, doi:10.1029/2003GB002069.

Hayley, K., L. R. Bentley, M. Gharibi, and M. Nightingale (2007), Low temperature dependence of electrical resistivity: Implications for near surface geophysical monitoring, *Geophys. Res. Lett.*, *34*, L18402, doi:10.1029/2007GL031124.

Hayley, K., L. R. Bentley, *and* M. Gharibi (2009), Time-lapse electrical resistivity monitoring of salt-affected soil and groundwater, *Water Resour. Res.*, *45*, W07425, doi:10.1029/2008WR007616.

Hilhorst, M. A. (2000), A pore water conductivity sensor, *Soil Sci. Soc. Am. J.*, *64*(6), 1922–1925, doi:10.2136/sssaj2000.6461922x.

Hodson, E. L., B. Poulter, N. E. Zimmermann, C. Prigent, and J. O. Kaplan (2011), The El Niño-Southern Oscillation and wetland methane interannual variability, *Geophys. Res. Lett.*, *38*, L08810, doi:10.1029/2011GL046861.

Johnson, T. C., L. Slater, D. Ntarlagiannis, F. D. Day-Lewis, and M. Elwaseif (2012), Monitoring groundwater-surface water interaction using time-series and time-frequency analysis of transient three-dimensional electrical resistivity changes, *Water Resour. Res.*, *48*, W07506, doi:10.1029/2012WR011893.

Kellner, E., A. J. Baird, M. Oosterwoud, K. Harrison, and J. M. Waddington (2006), The effect of temperature and atmospheric pressure on methane (CH_4) ebullition from near-surface peats, *Geophys. Res. Lett.*, *33*, L18405, doi:10.1029/2006GL027509.

Kettridge, N., A. Binley, S. M. Green, and A. J. Baird (2011), Ebullition events monitored from Northern Peatlands using electrical imaging, *J. Geophys. Res.*, *116*, G04004, doi:10.1029/2010JG001561.

Koestel, J., A. Kemna, M. Javaux, A. Binley, and H. Vereecken (2008), Quantitative imaging of solute transport in an unsaturated and undisturbed soil monolith with 3-D ERT and TDR, *Water Resour. Res.*, *44*, W12411, doi:10.1029/2007WR006755.

Krautblatter, M., and C. Hauck (2007), Electrical resistivity tomography monitoring of permafrost in solid rock walls, *J. Geophys. Res.*, *112*, F02S20, doi:10.1029/2006JF000546.

LaBrecque, D., and X. Yang (2001), Difference inversion of ERT data: Fast inversion method for 3-D in situ monitoring, *J. Environ. Eng. Geophys.*, *6*(2), 83–89.

LaBrecque, D. J., M. Miletto, W. Daily, A. Ramirez, and E. Owen (1996), The effects of noise on Occam's inversion of resistivity tomography data, *Geophysics*, *61*, 538–548.

Laing, C. G., T. G. Shreeve, and D. M. E. Pearce (2008), Methane bubbles in surface peat cores: In situ measurements, *Global Change Biol.*, *14*, 916–924, doi:10.1111/j.13652486.2007.01534.x.

Lowry, T., M. B. Allen, and P. N. Shive (1989), Singularity removal: A refinement of resistivity modeling techniques, *Geophysics*, *54*(6), 766–774, doi:10.1190/1.1442704.

Mastepanov, M., and T. R. Christensen (2009), Laboratory investigations of methane buildup in, and release from, shallow peats, in *Northern Peatlands and Carbon Cycling*, edited by A. J. Baird et al., pp. 205–218, AGU, Washington, D. C.

McDermitt, D., et al. (2011), A new low-power, open-path instrument for measuring methane flux by eddy covariance, *Appl. Phys. B*, *102*, 391–405.

McKenzie, J. M., D. I. Siegel, D. O. Rosenberry, P. H. Glaser, and C. I. Voss (2007), Heat transport in the Red Lake Bog, Glacial Lake Agassiz Peatlands, *Hydrol. Processes*, *21*, 369–378, doi:10.1002/hyp.6239.

Mitsch, W. J., and J. G. Gosselink (2007), *Wetlands*, John Wiley, Hoboken, N. J.

Moore, T. R., and M. Dalva (1993), The influence of temperature and water table position on carbon dioxide and methane emissions from laboratory columns of peatland soils, *J. Soil Sci.*, *44*, 651–664.

Osberg, P. H., A. M. Hussey II, and G. M. Boone (1985), *Bedrock geologic map of Maine, scale 1:500,000*, Maine Geol. Surv., Maine Dep. of Conserv., Augusta, Maine.

Ours, D. P., D. I. Siegel, and P. H. Glaser (1997), Chemical dilation and the dual porosity of humified bog peat, *J. Hydrol.*, *196*, 348–360.

Papa, F., C. Prigent, F. Aires, C. Jimenez, W. B. Rossow, and E. Matthews (2010), Interannual variability of surface water extent at the global scale, 1993–2004, *J. Geophys. Res.*, *115*, D12111, doi:10.1029/2009JD012674.

Parsekian, A. D., L. Slater, X. Comas, and P. H. Glaser (2010), Variations in free-phase gases in peat landforms determined by ground penetrating radar, *J. Geophys. Res.*, *115*, G02002, doi:10.1029/2009JG001086.

Parsekian, A. D., X. Comas, L. Slater, and P. H. Glaser (2011), Geophysical evidence for the lateral distribution of free-phase gas at the peat basin scale in a large northern peatland, *J. Geophys. Res.*, *116*, G03008, doi:10.1029/2010JG001543.

Parsekian, A. D., L. Slater, and D. Gimenéz (2012), Application of ground penetrating radar to measure near-saturation soil water content in peat soils, *Water Resour. Res.*, *48*, W02533, doi:10.1029/2011WR011303.

Ringeval, B., P. Friedlingstein, C. Koven, P. Ciais, N. de Noblet-Ducourdre, B. Decharmé, and P. Cadule (2011), Climate-CH_4 feedback from wetlands and its interaction with the climate-CO_2 feedback, *Biogeosciences*, *8*, 2137–2157, doi:10.5194/bg-8-2137-2011.

Romanowicz, E. A., D. I. Siegel, and P. H. Glaser (1993), Hydraulic reversals and episodic methane emissions during drought cycles in mires, *Geology*, *21*, 231–234.

Romanowicz, E. A., D. I. Siegel, J. P. Chanton, and P. H. Glaser (1995), Temporal variations in dissolved methane deep in the Lake Agassiz peatlands, Minnesota (USA), *Global Biogeochem. Cycles*, *9*, 197–212.

Rosenberry, D. O., P. H. Glaser, D. I. Siegel, and E. P. Weeks (2003), Use of hydraulic head to estimate volumetric gas content and ebullition flux in northern peatlands, *Water Resour. Res.*, *39*(3), 1066, doi:10.1029/2002WR001377.

Rosenberry, D. O., P. H. Glaser, and D. I. Siegel (2006), The hydrology of northern peatlands as affected by biogenic gas: Current developments and research needs, *Hydrol. Processes*, *20*, 3601–3610.

Siegel, D. I., J. P. Chanton, P. H. Glaser, L. S. Chasar, and D. O. Rosenberry (2001), Estimating methane production rates in bogs and landfills by deuterium enrichment of pore-water, *Global Biogeochem. Cycles*, *15*, 967–975.

Singha, K., F. D. Day-Lewis, T. Johnson, and L. D. Slater (2014), Advances in interpretation of subsurface processes with time-lapse electrical imaging, *Hydrol. Processes*, *29*, 1549–1576, doi:10.1002/hyp.10280.

Slater, L., and A. Reeve (2002), Understanding peatland hydrology and stratigraphy using integrated electrical geophysics, *Geophysics*, *67*, 365–378.

Slater, L., X. Comas, D. Ntarlagiannis, and M. R. Moulik (2007), Resistivity-based monitoring of biogenic gases in peat soils, *Water Resour. Res.*, *43*, W10430, doi:10.1029/2007WR006090.

Spahni, R., et al. (2011), Constraining global methane emissions and uptake by ecosystems, *Biogeosciences*, *8*(6), 1643–1665.

Stamp, I., A. J. Baird, and C. M. Heppell (2013), The importance of ebullition as a mechanism of methane (CH_4) loss to the atmosphere in a northern peatland, *Geophys. Res. Lett.*, *40*, 1–4, doi:10.1002/grl.50501.

Stocker, T. F., et al. (2013), Technical Summary, in *Climate Change 2013: The Physical Science Basis. Contribution of Working Group I to the Fifth Assessment Report of the Intergovernmental Panel on Climate Change*, edited by T. F. Stocker et al., pp. 33–115, Cambridge Univ. Press, Cambridge, U. K.

Strack, M., and T. Mierau. (2010), Evaluating spatial variability of free-phase gas in peat using ground-penetrating radar and direct measurement, *J. Geophys. Res.*, *115*, G02010, doi:10.1029/2009JG001045.

Ström, L., M. Mastepanov, and T. R. Christensen (2005), Species specific effects of vascular plants on carbon turnover and methane emissions from wetlands, *Biogeochemistry*, *75*, 65–82, doi:10.1007/s10533-004-6124-1.

Tokida, T., T. Miyazaki, and M. Mizoguchi (2005), Ebullition of methane from peat with falling atmospheric pressure, *Geophys. Res. Lett.*, *32*, L13823, doi:10.1029/2005GL022949.

Tokida, T., T. Miyazaki, M. Mizoguchi, O. Nagata, F. Takakai, A. Kagemoto, and R. Hatano (2007), Falling atmospheric pressure as a trigger for methane ebullition from peatland, *Global Biogeochem. Cycles*, *21*, GB2003, doi:10.1029/2006GB002790.

Waddington, J. M., K. Harrison, E. Kellner, and A. J. Baird (2009), Effect of atmospheric pressure and temperature on entrapped gas content in peat, *Hydrol. Processes*, *23*, 2970–2980, doi:10.1002/hyp.7412.

Walter, B. P., and M. Heimann (2000), A process-based, climate-sensitive model to derive methane emissions from natural wetlands: Application to five wetland sites, sensitivity to model parameters, and climate, *Global Biogeochem. Cycles*, *14*, 745–765, doi:10.1029/1999GB001204.

Webb, E. K., G. I. Pearman, and R. Leuning (1980), Correction of flux measurements for density effects due to heat and water vapour transfer, *Q. J. R. Meteorol. Soc.*, *106*, 85–100.

Yu, Z., L. D. Slater, K. V. R. Schäfer, A. S. Reeve, and R. K. Varner (2014), Dynamics of methane ebullition from a peat monolith revealed from a dynamic flux chamber system, *J. Geophys. Res. Biogeosci.*, *119*, 1789–1806, doi:10.1002/2014JG002654.